The nature of active Ni sites and the role of Al species in the oligomerization of ethylene on mesoporous Ni-Al-MCM-41 catalysts

Sara Moussa, Patricia Concepción, Maria A. Arribas, and Agustín Martínez*

Instituto de Tecnología Química, Universitat Politècnica de València - Consejo Superior de Investigaciones Científicas (UPV-CSIC), Avda. de los Naranjos s/n, 46022 Valencia, Spain.

*Corresponding author: amart@itq.upv.es (A. Martínez)

Abstract

Although nickel dispersed in mesoporous aluminosilicates are efficient catalysts for the oligomerization of ethylene, the nature of the active nickel sites still remains controversial. Here we applied in situ FTIR-CO spectroscopy during reaction with ethylene combined with reaction kinetics with online MS analysis of reaction products to unravel the nature of the active nickel species in *working* mesoporous Ni-Al-MCM-41 catalysts. The results revealed that isolated ion-exchanged Ni^{2+} cations are irreversibly blocked during the initial reaction stages leaving unsaturated Ni^{2+} cations grafted on silanols and at the surface of small (confined) NiO nanoparticles as the active species in the *pseudo*-steady state. The low activity of these species in pure silica materials suggested a promotional role of aluminum in the Al-MCM-41 matrix on enhancing the activity of Ni^{2+} sites, probably through a close interaction between Al species and nearby Ni^{2+} sites, as inferred from quantitative ^{27}Al MAS NMR and FTIR spectroscopies.

Keywords: ethylene oligomerization, Ni-Al-MCM-41 catalysts, active nickel sites, role of Al species.

1. INTRODUCTION

Higher olefins produced by the oligomerization of ethylene are valuable chemical intermediates in the manufacture of a variety of useful industrial products such as detergents, synthetic lubricants, plasticizer alcohols, and surfactants [1,2]. Moreover, the increasing availability of cheaper ethylene produced by cracking of ethane from shale gas and of renewable bio-ethylene from lignocellulosic bioethanol makes the oligomerization of ethylene even more attractive. Current commercial ethylene oligomerization processes operate in liquid phase at mild conditions using homogeneous catalysts based on transition metal (e.g., Ni, Co, Cr, Fe, etc.) complexes assisted by alkylaluminum co-catalysts or activators. Their replacement by more environmentally friendly heterogeneous systems is thus highly pursued albeit challenging.

Heterogeneous catalysts based on Ni dispersed on micro and mesoporous aluminosilicates are attracting considerable research interest as a green alternative to the current homogeneous systems [3]. As a general trend, nickel catalysts based on amorphous mesoporous aluminosilicates like silica-doped alumina, Al-MCM-41 and Al-SBA-15 exhibit higher activity, productivity to oligomers, and stability during reaction than Ni-zeolites displaying an essentially microporous character and stronger acid sites [4,5]. Indeed, Ni-zeolites tend to deactivate fast with time due to the blockage of micropores by bulky, highly branched oligomers formed on strong Brønsted acid sites. A notable exception to this behavior is the nanocrystalline Ni-beta zeolite reported by our group, for which no deactivation was observed during at least 10 h on stream in the oligomerization of ethylene at productive conditions due to an enhanced diffusion of oligomers within the nano-sized crystallites [6].

A differential aspect of the solid Ni-aluminosilicate catalysts is that they are able to perform the oligomerization of ethylene at moderate temperatures without the need of adding alkylaluminum activators as commonly required in homogeneous processes. This fact has generated an intense and interesting debate about the nature of the active nickel species and the reaction mechanism operating in Ni-aluminosilicates [3]. Although a definitive consensus on both issues has not yet been reached, a significant progress in the understanding of these fundamental questions has been achieved in the past years with the help of advanced in situ characterizations and theoretical (e.g. DFT) methods. The most controversial aspect in regards to the nature of active sites concerns the oxidation state of the nickel species. Thus, while Ni^0 [7], Ni^+ [8–11], and Ni^{2+} [4,6,12] were

proposed as active species in earlier works, more recent studies based on in situ FTIR experiments performed on Ni-beta [13] and on DFT calculations on Ni-SSZ-24 [14] advocate for isolated Ni^{2+} cations as the active species in Ni-zeolites. In these latter studies, the oligomerization reaction was concluded to occur, similarly to the homogeneous catalysts, through the classical Cossee-Arlman mechanism. Single-Event Microkinetic modeling studies did also support the Cossee-Arlman cycle as the most likely mechanism over amorphous mesoporous Ni-SiO_2-Al_2O_3 [15]. Alternatively, a mechanism involving metallacycle intermediates generated through the oxidative coupling of two ethylene molecules on a Ni site was postulated for the mesostructured Ni-Al-SBA-15 catalyst [16]. More recently, based on DFT-molecular dynamics simulation at operating conditions and microkinetic modelling, Olsbye et al. proposed as active site in zeolite Ni-SSZ-24 a reversible mobile $[(ethene)_2\text{-Ni-alkyl}]^+$ complex formed within the zeolite pores during reaction upon the exchange of two ethylene molecules with zeolite framework oxygens as nickel ligands [17]. This work, hence, establishes a connection between the active Ni species in homogeneous and heterogeneous Ni-based catalysts and allows accounting for their common Cossee-Arlman mechanism.

The isolated Ni^{2+} ions proposed as active sites in Ni-aluminosilicates were generally believed to be those at ion exchange positions compensating the negative framework charge induced by four-coordinated Al^{3+} species in bridged Si-O^--Al groups. In a recent work, we performed time-resolved in situ FTIR-CO experiments under flowing ethylene at 120 °C and 1 bar on Ni-beta to elucidate the nature of active nickel species in *working* Ni-beta zeolite [13]. We found that the ion-exchanged Ni^{2+} species, prevailing in the activated catalyst prior to reaction, became irreversibly blocked by hydrocarbon products since virtually the start of the reaction, leaving Ni^{2+} grafted on silanols $[Ni^{2+}\text{-}(SiO^-)_2]$ as the species responsible for the oligomerization activity of Ni-beta in the *pseudo*-steady state. The assignment of ion-exchanged Ni^{2+} ions as the only active species in Ni-aluminosilicates was also questioned in a previous study from our group comparing the activity for ethylene oligomerization of Ni dispersed on nanocrystalline beta zeolite and on amorphous mesoporous Al-MCM-41 and silica-doped alumina (Siralox-30) at similar Ni loading of 5 wt% [4]. In that work, we observed a remarkably higher activity for Ni-Al-MCM-41 and Ni-Siralox in spite of the much higher concentration of ion-exchanged Ni^{2+} ions in Ni-beta in comparison with Ni-Al-MCM-41 and of their absence in Ni-Siralox-30 after the thermal activation treatment.

On the above premises, in the present study we first performed an in situ time-resolved FTIR-CO study similar to that reported for Ni-beta in our previous work [13] to unravel the nature of active nickel species in Ni-Al-MCM-41 catalysts during catalysis. We will show that, as it occurs for Ni-beta, the ion-exchanged Ni^{2+} species are rapidly blocked and that only Ni^{2+} grafted on silanols and undercoordinated Ni^{2+} at the surface of very small NiO nanoparticles confined within the mesopores remain in the catalyst surface at steady state conditions. Then, it will be shown that, although these Ni species are not directly linked to Al, a close interaction of Al species with nearby Ni^{2+} cations is required to achieve high activity in ethylene oligomerization.

2. MATERIALS AND METHODS

2.1. Preparation of MCM-41 supports and Ni-based catalysts

The mesostructured Al-MCM-41 aluminosilicate (abbreviated here as Al-M41) with nominal Si/Al atomic ratio of 15 was synthesized according to the procedure reported in [18]. Briefly, the cationic surfactant hexadecyltrimethylammonium bromide (C_{16}TMABr) and aluminum hydroxide powder, used as Al source, were dissolved in a solution of tetramethylammonium hydroxide (TMAOH) at 40 ºC. Subsequently, the silica source (fumed silica, Aerosil 200, Degussa) was added to produce a gel with the following molar composition: SiO_2 : 0.15 C_{16}TMABr : 0.26 TMAOH : 0.0333 Al_2O_3 : 24.6 H_2O. The gel was aged for 1 h at room temperature, transferred to a Teflon-lined autoclave, and heated in static at 135 ºC for 24 h. The solid was recovered by filtration, washed with distillated water, dried at 60 ºC overnight, and calcined at 540 ºC (2 ºC/min) in flowing N_2 for 1 h and then in air for an additional 6 h period.

Additionally, a pure silica MCM-41 sample (referred to as Si-M41) was also synthesized following the procedure described above for Al-M41 excluding the addition of the Al source.

A series of Ni catalysts supported on the Al-MCM-41 carrier was prepared by incipient wetness impregnation of the pre-dried support with ethanolic solutions containing the required amounts of $Ni(NO_3)_2 \cdot 6H_2O$ precursor (Sigma-Aldrich, > 97% purity) to achieve nominal Ni loadings of 1, 3, 5, and 10 wt%. After impregnation, the samples were dried at 100 ºC overnight and calcined in air at 550 ºC for 3 h using a heating rate of 1 ºC/min.

The obtained catalysts are denoted as *x*Ni/Al-M41, where *x* stands for the nominal wt% Ni content.

A Ni catalyst dispersed in the all-silica Si-M41 support was prepared by grafting of Ni^{2+} ions from the Ni(II) amino complex solution $[Ni(NH_3)_x]^{2+}$ following a similar procedure to that reported in [19] for grafting Ni^{2+} on silica. Briefly, 2 g of Si-M41 support were suspended in 30 mL of a 0.02 M Ni^{2+} solution containing 2 wt% ammonia obtained by dissolving $Ni(NO_3)_2$ in a 2.0 M ammonia solution in methanol (Sigma-Aldrich). The mixture was vigorously stirred at room temperature for 1 h. The precipitate was filtered, washed with ethanol, dried at 60 ºC overnight, and then calcined in air at 350 ºC for 1 h (heating rate of 1 ºC/min). The obtained material was denoted as Ni-Si-M41 and contained 1.7 wt% Ni according to ICP-OES measurements. An additional Al-free Ni sample was similarly prepared but using, in this case, a 0.02 M Ni^{2+} aqueous solution containing 12.5 wt% ammonia obtained from $Ni(NO_3)_2$ and a 25% ammonia solution in water (Sigma-Aldrich). The precipitate was filtered, washed, dried, and air-calcined at the same conditions described above for Ni-Si-M41. The second treatment at more basic conditions was intentionally performed in order to provoke the partial dissolution and loss of structural pore ordering of the Si-M41 matrix and to produce a material comprising, after calcination, NiO nanoparticles as the only nickel species, as will be discussed later in the manuscript. The calcined sample is referred to as NiO-SiO_2 and contained 2.7 wt% Ni as determined by ICP-OES.

2.2. Characterization techniques

The Ni content and Si/Al ratio (for Al-containing materials) in the calcined Ni-containing catalysts were determined by Inductively Couple Plasma-Optimal Emission Spectrometry (ICP-OES) in a Varian 715-ES spectrometer after dissolution of the solids in an acid mixture of HNO_3:HF:HCl (1:1:3 volume ratio).

X-ray powder diffraction (XRD) patterns were recorded on a Philips X'Pert diffractometer using monochromatic CuK_α radiation (λ= 0.15405 nm), a scanning step of 0.03º, and counting time per step of 1 s.

Textural properties of the samples were derived from the respective N_2 adsorption isotherms measured at -196 ºC in an ASAP-2000 instrument (Micromeritics). Specific surface areas were calculated following the Brunauer-Emmett-Teller (BET) method, the

mesopore volumes (V_{meso}) was determined at a relative pressure of 0.85 (hence, excluding interparticle porosity), and the pore size distributions were obtained by applying the BJH algorithm using the Harkins-Jura reference curve and KJS correction [20]. Prior to the adsorption measurements, the samples were degassed at 400 ºC and vacuum overnight.

The acidic properties of parent Al-MCM-41 carrier and Ni-Al-MCM-41 catalysts were studied by FTIR spectroscopy of adsorbed pyridine on a Nicolet 710 FTIR apparatus. To this purpose, self-supported wafers of 10 mg/cm^2 were prepared and degassed at 400 ºC overnight under dynamic vacuum (10^{-6} mbar). Then, $1.8 \cdot 10^3$ Pa of pyridine were admitted to the IR cell and, after equilibration at room temperature (RT), the samples were degassed at 150 ºC, the corresponding spectrum recorded at RT, and the background spectrum subtracted. In a recent study, the integrated molar extinction coefficients of pyridine adsorbed on Brønsted acid sites (PyH^+), experimentally determined for four different zeolite topologies (FAU, BEA, MOR, MFI), were shown to depend, at a constant pyridine desorption temperature, of the specific zeolite structure [21]. Since the experimental molar absorption coefficients for PyH^+ species chemisorbed on mesostructured Al-MCM-41 and related materials are not available, we here compared the Brønsted acidity of the Al-MCM-41 and Ni/Al-MCM-41 samples on a relative basis using the integrated areas of the corresponding IR pyridine band at ca. 1545 cm^{-1} considering a value of 100 for the bare Al-MCM-41 carrier.

The reducibility of the nickel species was studied by hydrogen temperature-programmed reduction (H_2-TPR) in a Micromeritics Autochem 2910 device. The samples were initially flushed with Ar at RT for 30 min, and then the gas was switched to 10 vol% H_2 in Ar and the temperature linearly increased up to 900 ºC at a rate of 10 ºC/min. A downstream trap of 2-propanol in liquid nitrogen was used to retain the water formed during reduction while monitoring the H_2 consumption rate in a thermal conductivity detector (TCD) previously calibrated using the reduction of a standard CuO sample.

High-angle annular dark-field scanning transmission electron microscopy (HAADF-STEM) and transmission electron microscopy (TEM) images were obtained on a JEOL JEM-2100F apparatus operated at 200 kV. Prior to microscopy observation, the samples were dispersed in ethanol under ultrasonication, a drop was extracted from the top and deposited on a holey carbon-coated copper grid, and the solvent evaporated under ambient conditions. Fast Fourier Transform (FFT) analyses of lattice-resolved TEM images in selected samples were carried out using the Gatan Digital Micrograph software.

Histograms of particle size distribution for NiO species were generated for selected samples upon measurement of about 140 – 170 particles at several STEM micrographs taken at different positions on the grid. Specifically, 143, 168, and 152 particles were counted for the analyzed samples 1Ni/Al-M41, 5Ni/Al-M41, and 10Ni/Al-M41, respectively.

Solid-state ^{27}Al MAS NMR spectra were recorded on a Bruker AV 400WB spectrometer operating at 104.2 MHz and equipped with a 4 mm Bruker BL4 mm probe. Fully hydrated samples (ca. 40 mg) were packed into zirconia rotors and spun at the magic angle spinning (MAS) frequency of 10 kHz. The spectra were acquired at ambient temperature with pulses of 0.5 μs corresponding to a flip angle of $\pi/18$. Chemical shifts were referred to a 0.1 M aqueous solution of $Al(NO_3)_3$. For quantitative measurements, the spectra were normalized by weight of sample loaded into the rotor. Four spectra were acquired in each measurement to check the stability of the spectrometer.

Infrared spectra were recorded on a Nexus (Thermo) 8700 FTIR spectrometer using a DTGS detector and acquiring at a resolution of 4 cm^{-1}. A commercial Aabspec cell was used, allowing for in situ treatments under controlled atmospheres and temperatures from -176 to 500 ºC. Before spectra acquisition, the calcined supports and Ni-containing samples were pressed into self-supported wafers of ca. 10 mg/cm^2, introduced in the IR cell connected to a vacuum system, and thermally treated in situ at 300 °C for 3 h in flowing N_2 (20 cm^3/min), reproducing the in-reactor pretreatment conditions applied prior to catalysis. Afterwards, the temperature in the IR cell was decreased to 120 ºC (the temperature employed in the catalytic tests), and the nitrogen flow switched to pure ethylene. Next, the ethylene flow was stopped at selected reaction times (1 and 70 min) and the sample was immediately evacuated to 10^{-1} mbar using a rotatory pump and subsequently to 10^{-5} mbar with a turbomolecular pump while maintaining the temperature at 120 ºC for 1 h. At that moment, an FTIR spectrum was registered to study the nature and stability of the adsorbed species. Subsequently, the nature of the surface nickel species was assessed by titration with CO upon cooling the sample to -176 °C under dynamic vacuum of 10^{-5} mbar and dosing CO at increasing pressures from 0.14 to 2.0 mbar. The IR spectrum after each CO dose was then recorded. Assignation of IR components was done by the conventional curve fitting method. The IR spectra were deconvoluted using the Origin software, keeping the FWHM for a given peak constant between samples. For comparison, the IR spectra were normalized by sample overtone

area in the frequency range of 2104 – 1746 cm^{-1}. The analysis of IR peaks derived from the curve fitting approach was supported by performing the second derivative of selected IR spectra.

2.3. Catalytic experiments

2.3.1. Experiments at high pressure

The oligomerization of ethylene at productive high-pressure conditions were performed in a fixed bed stainless steel reactor loaded with ca. 0.4 g of catalyst pellets (0.2 – 0.4 mm) previously diluted with CSi granules (0.6 – 0.8 mm) to attain a constant bed volume of 6.5 cm^3, as detailed elsewhere [6]. Before reaction, the catalysts were pretreated in situ in flowing N_2 (50 cm^3/min) at 300 ºC for 16 h. The tests were carried out at 120 ºC, 35 bar total pressure (26 bar of ethylene balanced by Ar), and weight hourly space velocity (WHSV) of 10 h^{-1} in experiments lasting about 8 – 10 h. During the experiments, liquid oligomers were condensed in two traps located at the reactor outlet, weighted, and analyzed offline in a gas chromatograph (Bruker 450 GC) equipped with a capillary column (BR-1), two packed columns (Hayesep Q and Molecular Sieve 13 X), and two detectors (TCD and FID). Uncondensed products leaving the traps were periodically analyzed online in the same GC. The carbon number distribution of formed oligomers was obtained by merging the online and offline analyses. Carbon mass balances for the reported high-pressure experiments ranged 95 – 105%.

2.3.2. Experiments at ambient pressure

Additionally, ethylene oligomerization experiments were also carried out in a fixed bed glass microreactor loaded with ca. 100 mg of catalyst pellets (0.2 – 0.4 mm) diluted with CSi granules (0.6 – 0.8 mm) to attain a constant bed volume of 1 cm^3. Prior to reaction, the catalysts were pretreated in situ under flowing N_2 (20 cm^3/min) at 300 ºC for 3 h. The experiments, lasting about 100 min, were carried out at differential conditions (ethylene conversions < 10%) at a temperature of 120 ºC, a total pressure of 1 bar (0.95 bar of ethylene balanced with Ar, used as internal GC standard), and a space velocity (WHSV) of 33 h^{-1} [13]. The reaction products were qualitatively followed by online mass spectrometry (MS) in the multi-ion mode for preselected m/z fragmentations (m/z = 26 for ethylene, m/z = 56 for butenes, and m/z = 84 for hexenes) using a Balzer (QMG 220M1, Onmistar) mass spectrometer. The employed microreactor-MS setup, having a

minimum dead volume, allowed for the continuous monitoring of products since virtually zero time on stream. For quantitative analyses, the gaseous stream at the reactor outlet was collected in sample bags at selected reaction times and analyzed offline in the Bruker 450 GC gas chromatograph described above for the high-pressure runs. At the differential conditions employed in the ambient pressure experiments (i.e. low ethylene conversions), carbon mass balances were in all cases better than 98%.

2.3.3. Reproducibility of catalytic experiments

Duplicated experiments with selected *x*Ni/Al-M41 catalysts were performed at the beginning of the study in order to confirm the good reproducibility of the catalytic data at both high and ambient pressure conditions (Fig. S1).

3. RESULTS AND DISCUSION

3.1. Characterization of catalysts

3.1.1. Structural and textural characterization

The atomic Si/Al ratio for both the calcined Al-M41 support and the *x*Ni/Al-M41 catalysts was 13, as measured by ICP-OES. The Ni content (ICP-OES), textural properties (N_2 physisorption), and Brønsted acidity (FTIR-pyridine) of the materials are gathered in Table 1. The Ni contents of the impregnated *x*Ni/Al-M41 samples agreed well with the nominal values. The presence of the (100) reflection at 2.1° (2θ) in the low-angle XRD patterns (Fig. S2) and the type-IV N_2 adsorption isotherms with a narrow pore size distribution (Fig. S3), characteristic of mesostructured solids, indicated a relatively high long-range hexagonal ordering of mesopores in both Al-M41 and *x*Ni/Al-M41 samples. This is also supported by the high BET surface areas exhibited by these materials (781 – 923 m^2/g), as shown in Table 1.

Table 1. Ni content, textural properties, and relative Brønsted acidity of Al-M41 support and impregnated *x*Ni/Al-M41 catalysts.

Sample	Ni content (wt%)	BET area (m^2/g)	V_{meso}[a] (cm^3/g)	APD[b] (nm)	Relative Brønsted acidity[c]
Al-M41	-	923	0.79	3.77	100
1Ni/Al-M41	1.3	901	0.76 (0.77)	3.65	69
3Ni/Al-M41	2.8	880	0.74 (0.77)	3.63	53
5Ni/Al-M41	5.7	829	0.68 (0.73)	3.54	56
10Ni/Al-M41	9.8	781	0.61 (0.70)	3.54	50

[a] Volume of mesopores. Values in parenthesis are the mesopore volumes normalized per mass of support.
[b] Average pore diameter.
[c] Relative amounts of Brønsted acid sites at a pyridine desorption temperature of 150 °C, taking the value for the Al-M41 support as 100.

Moreover, it can be seen in Table 1 that the Ni-containing catalysts showed lower average pore diameters (3.54 – 3.65 nm) and mesopore volumes normalized per mass of support (0.70 – 0.77 cm^3/g) in comparison with the pristine Al-M41 (mean pore size of 3.77 nm and mesopore volume of 0.79 cm^3/g). These observations are suggestive of a partial plugging of pores due to the presence of NiO nanoparticles within the mesochannels. In turn, the fact that both the mean pore diameter and normalized mesopore volume gradually decreased with the Ni content signs for a higher amount of confined NiO nanoparticles at higher Ni loadings.

The high-angle XRD patterns of the catalysts (Fig. S4) showed very weak and broad reflections at about 37º, 43º, and 63º (2θ) corresponding, respectively, to the (111), (200), and (220) crystal planes of the *fcc*-NiO phase (JCPDS 04-0835) only for the catalysts loaded with 5.7 and 9.8 wt% Ni. The absence of NiO reflections at lower Ni contents suggests that the size of NiO crystallites in these samples should be below the detection limit of the technique (3 – 4 nm).

Hydrogen temperature-programmed reduction (H_2-TPR) experiments were performed to obtain information on the type of Ni species present in the catalysts according to their reducibility. The corresponding H_2-TPR profiles are shown in Fig. 1. Three main reduction regions can be distinguished: T < 350 ºC (I), 400 < T < 600 ºC (II), and T > 650 ºC (III). Hydrogen consumptions in the low-temperature range (region I) are

associated to the reduction bulk-like NiO nanoparticles displaying low interaction with the support [22] which, in our catalysts, should reside at the external surface of the Al-M41 carrier. This assignment is supported by the single reduction peak at ca. 278 ºC observed in the H_2-TPR profile of bulk (30 nm in size) NiO particles physically mixed with Al-MCM-41 to achieve a Ni content of 5 wt% Ni (Fig. S5). On the other hand, hydrogen consumptions at high temperatures (region III) in Ni-aluminosilicates are attributed to the reduction of highly dispersed Ni cations strongly interacting with the aluminosilicate matrix. The broad reduction feature at temperatures above 600 °C suggests the presence of more than one type of nickel species reducing in this region. In fact, as observed in the deconvoluted H_2-TPR profiles shown in Fig. S6, two components peaking at about 625 and 750 °C, respectively, were evidenced in region III. The peak at ca. 750 °C is associated with the reduction of Ni^{2+} in ion exchange positions [22–24], while that at around 625 °C can be tentatively attributed to the reduction of the grafted Ni^{2+} species [25]. Moreover, reduction features at intermediate temperatures (region II) in Ni catalysts supported on MCM-41 materials are assigned to the reduction of very small NiO nanoparticles located within the mesochannels [26,27]. As inferred from the reduction profiles in Fig. 1, the later are the most abundant nickel species in the impregnated catalysts, particularly at Ni loadings > 2 wt%. The increase in the H_2 consumption in region II and the concomitant shift of the peak maximum towards higher temperatures (466 ºC $\rightarrow$ 528 ºC) indicates that the amount of in-pore NiO nanoparticles and their average interaction strength with the Al-M41 walls raises at increasing Ni contents. Thus, besides shedding some light on the Ni speciation in our Ni-containing catalysts, the H_2-TPR results show that the impregnation and calcination conditions employed for preparing the *x*Ni/Al-M41 catalysts were effective to confine most of NiO nanoparticles within the mesochannels even at Ni loadings as high as ca. 10 wt%.

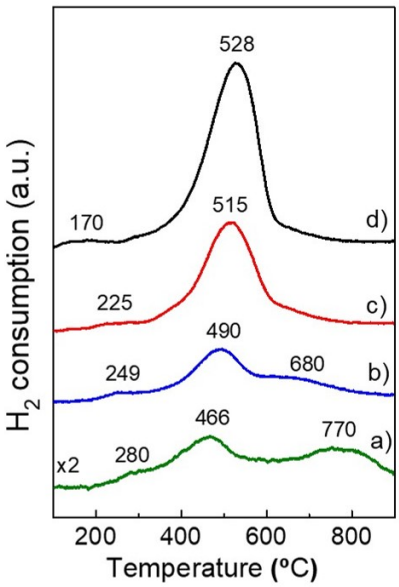

Fig. 1. H_2-TPR profiles for the calcined xNi/Al-M41 catalysts with nickel loadings of 1.3 (a), 2.8 (b), 5.7 (c), and 9.8 wt% (d).

The presence of NiO nanoparticles in the impregnated xNi/Al-M41 catalysts even at low Ni loading was directly evidenced by electron microscopy. Representative HAADF-STEM images along with their corresponding NiO particle size histograms are presented in Fig. 2 for samples 1Ni/Al-M41, 5Ni/Al-M41, and 10Ni/Al-M41. Abundant small NiO nanoparticles, appearing as bright spots in the images, are clearly observed. FFT analysis of a representative TEM image of 1Ni/Al-M41 (Fig. S7) indicates that the NiO nanoparticles crystallized in a face-centered cubic (*fcc*) phase, in agreement with the crystalline NiO phase detected by XRD for the high loaded 5Ni/Al-M41 and 10Ni/Al-M41 samples (Fig. S4). As seen in the histograms, the NiO nanoparticles exhibited a relatively narrow particle size distribution with a mean particle size that progressively raised from 2.6 to 3.8 nm as the Ni content increased from 1.3 to 9.8 wt%. The fact that the size of most of the NiO particles in samples loaded with 1.3 and 5.7 wt% Ni fell in the range of 2 to 4 nm, practically matching the pore size distribution of the Al-M41 carrier (Fig. S3b), suggests that they should mainly reside within the mesopores. At the highest loading of 9.8 wt%, however, about 30% of the nanoparticles showed sizes above 4 nm and should, therefore, locate at the external surface of the Al-M41 grains.

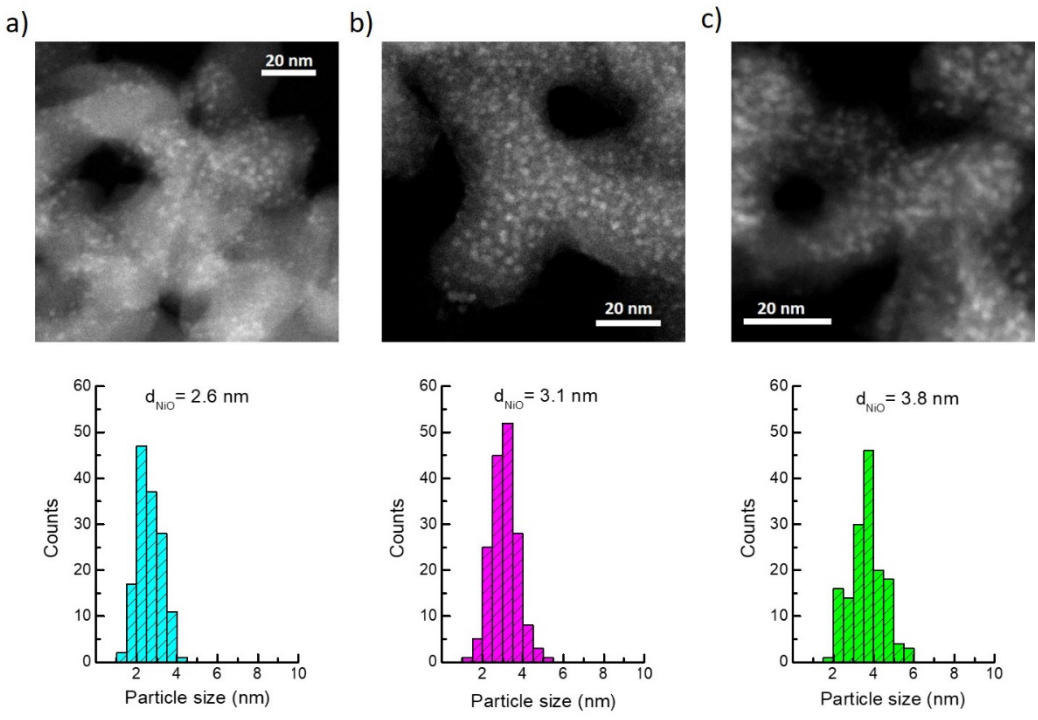

Fig. 2. Representative HAADF-STEM images for the impregnated xNi/Al-M41 catalysts loaded with 1.3 (a), 5.7 (b), and 9.8 wt% Ni (c). The corresponding particle size histograms are shown at the bottom of each image.

As for acidity, the impregnation of Al-M41 with the nickel precursor and subsequent calcination produced a reduction of the density of Brønsted acid sites (Table 1) due mainly to the partial exchange of H^+ with Ni^{2+} cations, as also observed in previous studies for different Ni-aluminosilicates prepared by impregnation [6,23]. As observed in Table 1, the relative amount of Brønsted acid sites decreased by about 50% with increasing the Ni content up to 2.8 wt% and then remained practically constant at higher loadings, suggesting that the amount of ion-exchanged Ni^{2+} species did not further increase above this nickel loading. Nevertheless, the conclusion about the degree of ion exchange of protons by Ni^{2+} species based on IR-pyridine measurements should be taken with caution due to several factors. On one hand, it is likely that not all the Brønsted acid sites capable of being exchanged by Ni^{2+} cations are titrated by pyridine at a desorption temperature of 150 °C. On the other hand, the partial blockage of pores by confined NiO nanoparticles, especially at high Ni loading (Table 1), may hinder the access of pyridine to a fraction of the acid sites located within the mesopores.

3.1.2. Surface nickel species in activated xNi/Al-M41 catalyst studied by FTIR-CO

Low-temperature FTIR of adsorbed CO is a highly sensitive technique to study the oxidation state and chemical environment of surface metal species. Here we first performed FTIR-CO at -176 °C to elucidate the nature of surface Ni species in the impregnated *x*Ni/Al-M41 catalysts after the thermal activation treatment at 300 ºC in N_2 flow applied prior to catalysis. The IR spectra at CO saturation (2 mbar) for the bare Al-M41 carrier and the impregnated *x*Ni/Al-M41 samples with different nickel loadings are shown in Fig. 3. All Ni-containing catalysts exhibited three main IR bands with maxima at 2197, 2174, and 2157 cm^{-1}, along with an additional band at 2134 cm^{-1} due to physisorbed CO (Fig. 3b-e). The IR bands at 2174 and 2157 cm^{-1}, also present in the spectrum of the pristine Al-M41 carrier (Fig. 3a), have been assigned to CO interacting with, respectively, Brønsted acid sites and silanol groups [28,29]. On the other hand, the component at 2197 cm^{-1} is related to CO interacting with Ni^{2+} species [4,30]. Worth of mention is the lack of IR bands of $Ni^{+}(CO)_2$ dicarbonyls at 2138 and 2096 cm^{-1} and/or of Ni^{+}-CO monocarbonyls at 2113 cm^{-1} [29], which clearly manifests the absence of monovalent Ni^{+} cations in the activated *x*Ni/Al-M41 catalysts. Based on the asymmetry and the evolution of the IR band at 2197 cm^{-1} at increasing CO coverages (Fig. S8a), the existence of four Ni^{2+}-related components with maxima at ca. 2207, 2197, 2185 and 2174 cm^{-1} could be identified, as supported by the second derivative curves shown in Fig. S8b. As an example, the deconvoluted spectrum of the 5Ni/Al-M41 sample is shown in the inset of Fig. 3. The distinct CO vibration frequency of the Ni^{2+}−CO complexes evidences the presence of Ni^{2+} ions in different local environments exhibiting dissimilar Lewis acid strength (i.e., electron-accepting capability). Hence, the high frequency component at 2207 cm^{-1} is ascribed to isolated Ni^{2+} ions in ion exchange positions (i.e., exchanging protons in bridged Si-OH-Al groups) [4,13,30–32]. According to their frequency, these species exhibit the strongest Lewis acid character among the detected Ni^{2+} species, and are those widely assumed as the active nickel sites in Ni-aluminosilicates. Furthermore, the IR band at 2197 cm^{-1} is associated with isolated grafted Ni^{2+} species formed by reaction with defective silanol groups and subsequent removal of water ligands by thermal treatment, resulting in coordinatively unsaturated Ni^{2+} cations bound to the support surface through framework oxygen atoms [Ni^{2+}-$(SiO^{-})_2$] [4,13,19,30]. On the other hand, the band peaking at about 2185 cm^{-1} is related to CO adsorbed on coordinatively unsaturated Ni^{2+} species at the surface of small NiO nanoparticles [4]. It

should be pointed out that, although as mentioned before the component at 2174 cm^{-1} present in the spectrum of the Al-M41 support (Fig. 3a) is associated with CO adducts with Brønsted acid sites, the Ni^{2+} species in small NiO nanoparticles do also contribute to this band. This is corroborated by the presence of this band in the IR-CO spectrum of an Al-free Ni/Si-MCM-41 sample lacking Brønsted acidity (Fig. S9). The lower IR frequencies of the NiO-related bands indicate that these Ni^{2+} species have weaker Lewis acidity in comparison with those in ion exchange positions and grafted on silanols.

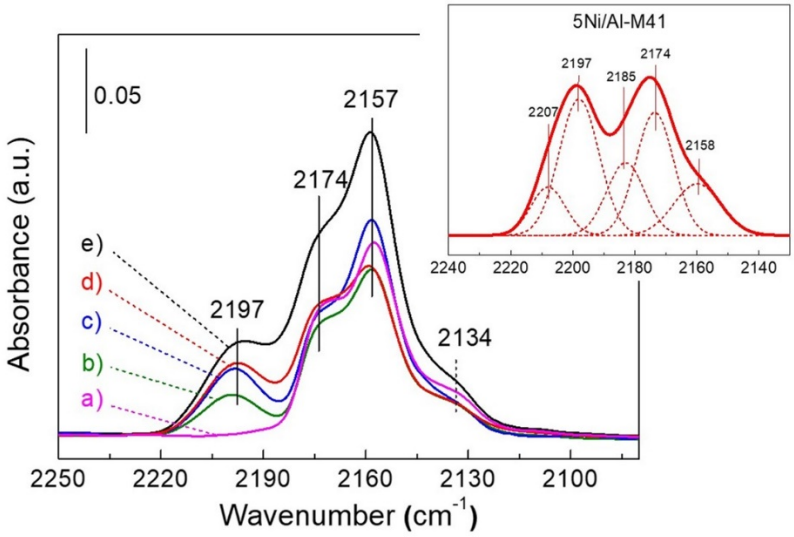

Fig. 3. FTIR-CO spectra at CO saturation (2 mbar) for the bare Al-M41 carrier and the impregnated *x*Ni/Al-M41 catalysts after thermal treatment in flowing N_2 at 300 ºC: a) Al-M41, b) 1Ni/Al-M41, c) 3Ni/Al-M41, d) 5Ni/Al-M41, and e) 10Ni/Al-M41. The inset shows the deconvoluted spectrum of the 5Ni/Al-M41 sample at an intermediate CO coverage.

The evolution with Ni loading of the different surface Ni^{2+} species present in *x*Ni/Al-M41 catalysts, derived from the area of the respective IR bands in the normalized deconvoluted spectra, is shown in Fig. S10. As observed, the amount of ion-exchanged Ni^{2+} species (band at ca. 2207 cm^{-1}) increased with increasing the Ni loading from 1.3 to 2.8 wt%, slightly declined with the increment in Ni content up to 5.7 wt%, and then remained practically constant with the further increase in Ni loading up to 9.8 wt%. Moreover, the amount of Ni^{2+} ions grafted in silanols (band at 2197 cm^{-1}) showed a maximum for the sample loaded with 5.7 wt% Ni, while that of Ni^{2+} in small NiO nanoparticles (band at

2185 cm^{-1}) raised continuously with Ni loading, in agreement with the trend observed for the reduction of in-pore NiO nanoparticles in the H_2-TPR profiles (Fig. 1).

3.2. Oligomerization of ethylene on Ni-Al-MCM-41 catalysts

As detailed in Experimental, the ethylene oligomerization experiments were carried out at differential conditions in a microreactor at 120 °C, 1 bar total pressure (0.95 bar ethylene, Ar as balance gas), and WSHV of 33 h^{-1}. During the experiments, the reaction products were continuously monitored by online mass spectrometry (MS), enabling a high temporal resolution since the very early stages of the reaction. At these conditions, dimerization of ethylene was the main reaction occurring on the *x*Ni/Al-M41 catalysts resulting in a high selectivity of butenes of ca. 90% (Table S1). Moreover, preliminary blank experiments indicated that the bare Al-M41 support was not active and, therefore, that Brønsted acid sites are unable to activate and oligomerize ethylene at the studied conditions. The lack of activity at moderate temperatures (< 200 °C) in the absence of nickel species has also been reported in earlier studies for different acidic zeolites [4,33,34] and mesoporous aluminosilicates [22,35], and was rationalized considering that the oligomerization of ethylene catalyzed by Brønsted acid sites would involve energetically unfavorable primary carbocation intermediates. In consequence, the activity of the Ni-containing catalysts in this work is exclusively ascribed to the active Ni species. The evolution with time of the intensity of the mass spectral signal of butenes (m/z = 56) for the *x*Ni/Al-M41 catalysts loaded with different amounts of Ni is shown in Fig. 4. Regardless the Ni loading, all catalysts experienced a rapid loss of activity during the first 20 min on stream followed by a *pseudo*-steady state period where the formation rate of butenes remained nearly constant until the completion of the experiment. The qualitative behavior with time on stream (TOS) and the activity trend with Ni loading inferred from the butenes signal in the online MS analyses reproduced well those observed for the ethylene conversion derived from the quantitative offline GC analyses, as shown in Fig. S11. In both cases, the activity significantly raised with the increase in Ni content from 1.3 to 5.7 wt% and then increased very slightly with the further increase in loading up to 9.8 wt%. We notice that an alike behavior was observed for Ni/beta zeolite catalysts tested in the same reactor setup at identical reaction conditions [13].

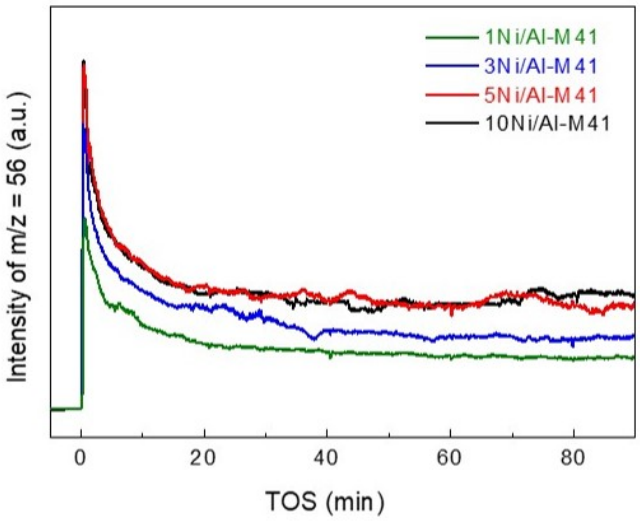

Fig. 4. Evolution of the mass spectral signal of butenes (m/z = 56) with TOS for *x*Ni/Al-M41 catalysts. Reaction conditions: 120 °C, 1 bar total pressure (0.95 bar ethylene + 0.05 bar Ar), and WHSV of 33 h^{-1}.

The catalytic performance of the *x*Ni/Al-M41 catalysts was also assessed at more industrially relevant high-pressure conditions (120 °C, 35 bar total pressure, and WHSV of 10 h^{-1}) as detailed in Experimental. It is worth mentioning that in these experiments, where the first reliable analysis of products in the online GC was performed after about 1 h on stream, the initial transient behavior observed at ambient pressure (Fig. 4, Fig. S11a) could not be captured and the catalysts apparently exhibited a relatively stable activity with TOS (Fig. S12). Nevertheless, at 35 bar, the conversion of ethylene after about 8 – 10 h on stream (*pseudo*-steady state) gradually increased from 42% for 1Ni/Al-M41 to 93% for 10Ni/Al-M41 (Fig. 5a). The raise in ethylene conversion with Ni loading was accompanied by a decline in the selectivity of butenes from 61 to 42% and a concomitant raise in the selectivity of higher (C_{5+}) oligomers, as shown in Table S2 of Supporting Information. The results in Fig. 5a thus revealed the same reactivity trend with Ni content for the experiments performed at 1 and 35 bar. In fact, despite the conversion rates at 35 bar were about one order of magnitude higher than at 1 bar, there was a good linear correlation (R^2 = 0.994) between the *pseudo*-steady state conversion rates at both conditions (Fig. 5b), as also found for Ni/beta in our previous study [13].

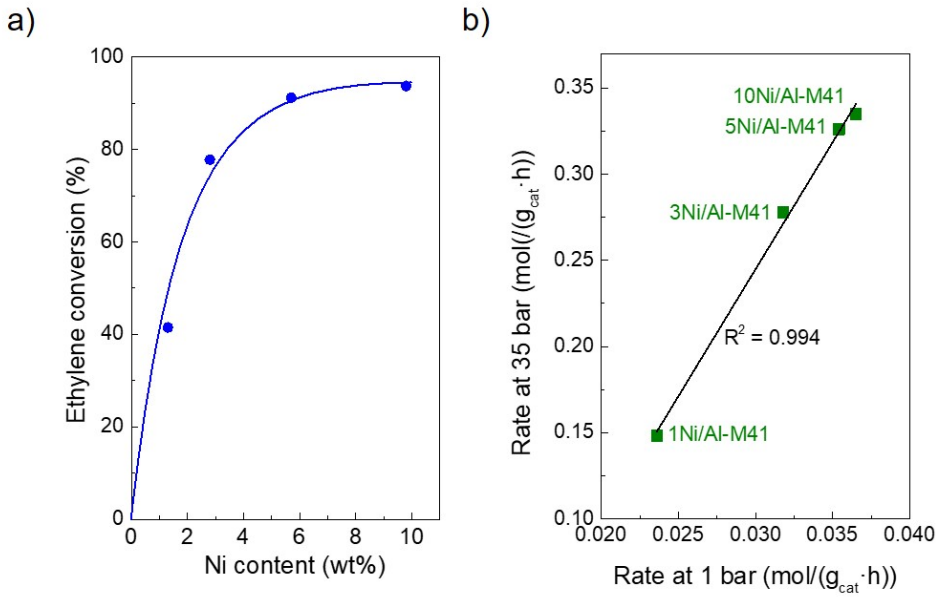

Fig. 5. a) Ethylene conversion in the *pseudo*-steady state (TOS = 8 – 10 h) as a function of Ni loading for *x*Ni/Al-M41 catalysts at high-pressure conditions (120 °C, 35 bat total pressure, WHSV = 10 h^{-1}); b) linear correlation between the ethylene conversion rates at 1 and 35 bar total pressure.

The above results strongly point towards the same type of active nickel species operating in the *working* *x*Ni/Al-M41 catalysts regardless of the reaction pressure and, therefore, validate the use of FTIR-CO experiments at ambient pressure to elucidate their nature. At this point, it should be highlighted that the activity of the *x*Ni/Al-M41 catalysts at both 1 bar and 35 bar continued increasing at Ni contents well above that corresponding to the maximum theoretical ion exchange capacity of the Al-M41 carrier which, as mentioned beforehand, was estimated at 2.4 wt% Ni. Obviously, this trend can hardly be explained considering the ion-exchanged Ni^{2+} cations as the only active species as widely assumed. This aspect is addressed in the next section based on time-resolved in situ FTIR-CO spectroscopy.

3.3. Nature of active nickel species in Ni-Al-MCM-41 catalysts

3.3.1. Time-resolved in situ FTIR spectroscopy

The nature of active Ni species under working conditions was investigated by means of FTIR spectroscopy using CO as probe molecule after in situ reaction of *x*Ni/Al-M41 catalysts with ethylene in the IR cell at 120 °C and atmospheric pressure. The FTIR spectra at CO saturation of Ni-carbonyl bands for the 5Ni/Al-M41 catalyst after the thermal pretreatment with N_2 at 300 °C (considered as TOS = 0) and after 1 and 70 min of reaction are presented in Fig. 6. The presence of the different IR components, and particularly the less intense band at 2185 cm^{-1}, is clearly evidenced in the respective deconvoluted spectra and is further supported by the second derivative approach, as exemplified in Fig. S13 for the spectrum recorded after 70 min of in situ reaction with ethylene.

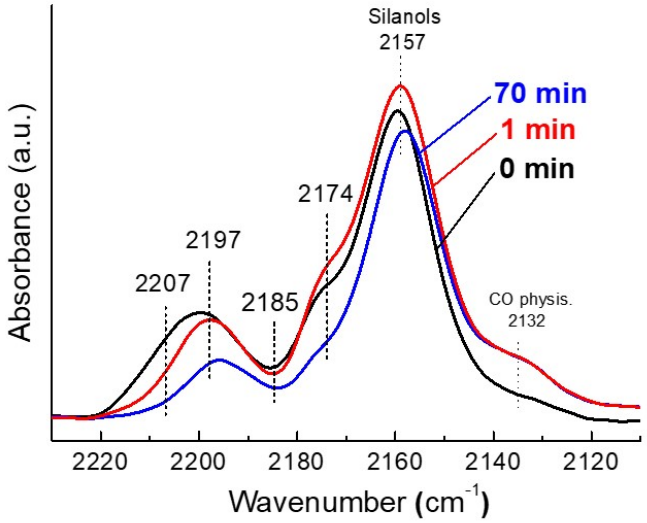

Fig. 6. FTIR spectra at CO saturation of Ni-carbonyl bands for 5Ni/Al-M41 catalyst after the pretreatment in N_2 at 300 °C (0 min) and after 1 and 70 min of in situ reaction with ethylene at 120 ºC and 1 bar.

As observed, the IR band at 2207 cm^{-1} related to ion-exchanged Ni^{2+} ions experienced a significant reduction in intensity already after 1 min of reaction and virtually vanished after 70 min corresponding to the *pseudo*-steady state period. Comparatively, the IR bands associated to isolated Ni^{2+} ions grafted on silanols (2197 cm^{-1}) and to undercoordinated Ni^{2+} on the surface of small NiO nanoparticles (2185 cm^{-1}) were much less affected and their intensity was preserved to a large extent after 70 min of reaction

(Fig. 6). The same behavior was observed for all *x*Ni/Al-M41 samples irrespective of the Ni loading, as exemplified in Fig. S14 for the catalyst loaded with 2.8 wt% Ni (3Ni/Al-M41).

Furthermore, the parallelism between the decline in the intensity of the Ni^{2+}-related IR bands, particularly the band of the most acidic ion-exchanged species at 2207 cm^{-1}, and the initial loss of activity observed in the catalytic experiments at 1 bar (Fig. 4) is suggestive of a common origin for both behaviors. In this regard, it is worth noting that, concomitantly to the decrease in intensity of the Ni^{2+} carbonyl bands, new IR bands in the C-H vibration region characteristic of CH_3 and CH_2 groups developed, as illustrated in Fig. S15 for 5Ni/Al-M41. The fact that these bands persisted after evacuation of the cell at 120 °C for 1 h under dynamic vacuum of 10^{-5} mbar signs for the formation of strongly adsorbed acyclic hydrocarbon species playing the role of spectators. Therefore, our results collectively indicate that the fast initial activity decline (Fig. 4 and Fig. S11a) originated mainly from the rapid blockage of the ion-exchanged Ni^{2+} ions by irreversibly adsorbed C_xH_y species, as it was also concluded for zeolite Ni/beta [13]. This, besides the fast initial decline in activity, suggest that the ion-exchanged nickel species, which exhibit the strongest Lewis acidity, should be contributing the most to the high initial (at TOS = 0) activity of the *x*Ni/Al-M41 catalysts.

Based on the results discussed beforehand, we here suggest that isolated Ni^{2+} cations grafted on silanols and at the surface of small NiO nanoparticles confined within the mesopores are those mainly responsible for the ethylene oligomerization activity of *x*Ni/Al-M41 catalysts in the *pseudo*-steady state rather than the commonly accepted ion-exchanges ones. The milder Lewis acidity of the former species prevents a too strong adsorption of hydrocarbon intermediates and/or products and consequently their rapid blockage under reaction conditions.

3.3.2. Ni catalysts based on pure silica materials

Considering the nature of the suggested active nickel species in Ni-Al-MCM-41 catalysts, it comes the obvious question of whether or not the presence of Al species in the carrier is required for the activation and oligomerization of ethylene on heterogeneous Ni-based catalysts. To address this question, two Al-free nickel catalysts were prepared by grafting as described in section 2.1 under Experimental, namely Ni-Si-M41 and NiO-SiO_2 containing, respectively, 1.7 and 2.7 wt% Ni. The low-angle XRD pattern of Ni-Si-M41 (Fig. S16a) shows narrow and well-resolved (100), (110), and (200) reflections, indicative

of a high structural ordering of the hexagonally arranged mesopores. By contrast, the NiO-SiO_2 sample exhibits a poorly ordered structure, with only a very low intense (100) reflection being visible in its low-angle XRD pattern (Fig. S16a), due to the partial dissolution of silica and consequent loss of pore ordering in the Si-MCM-41 carrier caused by the more severe basic conditions applied in its preparation (section 2.1). Moreover, a high dispersion of nickel species in both Al-free samples is inferred from the absence of NiO-related reflections in their respective high-angle XRD patterns (Fig. S16b).

The nickel speciation in these samples after activation in flowing N_2 at 300 °C for 3 h was studied by low-temperature FTIR-CO. The corresponding deconvoluted spectra in the Ni-carbonyl region are presented in Fig. 7. As expected from the absence of Al in these samples, their FTIR-CO spectra lack the component of ion-exchanged Ni^{2+} species at 2207 cm^{-1}. It can also be seen that Ni-Si-M41, with an ordered mesoporous structure, presents the IR bands associated to Ni^{2+} ions both grafted on silanols (2191 cm^{-1}) and at the surface of small NiO nanoparticles (2183 and 2174 cm^{-1}). Distinctly, the non-ordered NiO-SiO_2 sample exhibits only the IR bands of small NiO nanoparticles at 2183 and 2174 cm^{-1}. According to STEM (Fig. S17), the size of NiO nanoparticles in NiO-SiO_2 (2 – 5 nm) was similar to that of NiO in *x*Ni/Al-M41 (Fig. 2). Interestingly, the IR bands of grafted Ni^{2+} species and of small NiO nanoparticles in Ni-Si-M41 and NiO-SiO_2 appeared shifted towards lower frequencies compared with the equivalent bands in the Al-containing *x*Ni/Al-M41 catalysts peaking at, respectively, 2197 and 2185 cm^{-1} (Fig. 3). A similar behavior was observed for the Ni^{2+}-CO band at 2197 cm^{-1} in Ni catalysts dispersed on Al-beta and Si-beta zeolites [36]. Notice that a fair comparison of the frequency of the NiO component at ca. 2174 cm^{-1} between the pure silica and the Al-containing samples cannot be made due to its overlapping with the strong IR band of CO adducts with Brønsted acid sites in the later. Moreover, the IR band of Ni^{2+} grafted on silanols experienced a larger blue shift (6 cm^{-1}) than that of Ni^{2+} in sub-4 nm NiO (2 cm^{-1}) when present in the pure-silica carriers. The lower frequency of the Ni^{2+}-CO IR bands indicates that the associated Ni^{2+} species in the Al-free samples exhibit a weaker Lewis acidity (i.e., a lower electrophilic character) than when present in the aluminosilicate Al-M41 support.

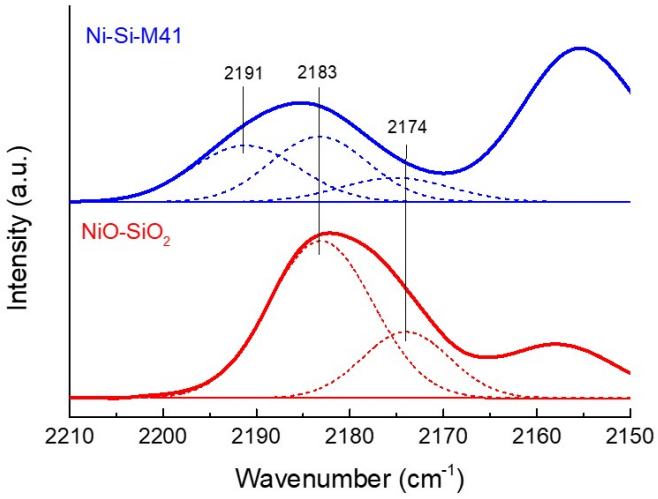

Fig. 7. Deconvoluted FTIR spectra in the nickel carbonyl region at intermediate CO coverage for Al-free Ni-Si-M41 and NiO-SiO_2 samples after thermal treatment in flowing N_2 at 300 ºC for 3 h.

Next, the ethylene oligomerization activity of the Al-free Ni-based catalysts was assessed in the microreactor-MS setup at 120 °C, 1 bar total pressure (0.95 bar ethylene balanced by Ar), and WSHV of 33 h^{-1}. The evolution with TOS of the intensity of the mass spectral signal of butenes (m/z = 56) for Ni-Si-M41 and NiO-SiO_2 samples is presented in Fig. 8 and confronted against the results obtained for the low-loaded 1Ni/Al-M41 catalyst displaying the lowest activity among the impregnated *x*Ni/Al-M41 series (Fig. 3). In comparison with 1Ni/Al-M41, the two Al-free samples were remarkably less active. Among the two Al-free materials, Ni-Si-M41 comprising both Ni^{2+} grafted on silanols and small NiO nanoparticles showed a higher activity than NiO-SiO_2 containing small NiO nanoparticles as the only nickel species, in spite of the higher Ni content in the later. From these results, one might conclude that the reactivity of Ni^{2+} grafted on silanols should be higher than that of small NiO nanoparticles, a trend that seems compatible with the higher Lewis acidity of the former species inferred from the higher frequency of the associated IR band (2197 *vs.* 2185 cm^{-1}). Unfortunately, the lack of molar extinction coefficients for the corresponding nickel-carbonyl IR bands prevents us to quantify the amount of each type of Ni^{2+} species accessible on the surface of catalysts and, therefore, to establish a fair comparison of their intrinsic reactivity (per Ni site) towards ethylene. Furthermore, the results in Fig. 8 evidenced a higher reactivity in the *pseudo*-steady state

of the Ni^{2+} species grafted on silanols and at the surface of small NiO nanoparticles when dispersed in the aluminosilicate Al-MCM-41 matrix in comparison with the pure silica carriers.

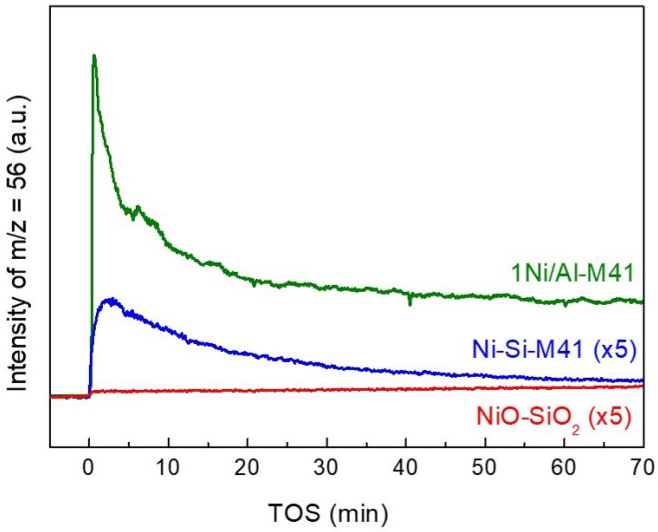

Fig. 8. Evolution of the mass spectral signal of butenes (m/z = 56) with TOS for the Al-free Ni-Si-M41 (1.7 wt% Ni) and $NiO\text{-}SiO_2$ (2.7 wt% Ni) samples. For comparative purposes, the curve for the 1Ni/Al-M41 catalyst (1.3 wt% Ni) is also included. Reaction conditions: 120 °C, 1 bar total pressure (0.95 bar ethylene + 0.05 bar Ar), and WHSV of 33 h^{-1}.

3.3.3. Interaction between Ni and Al species in Ni-Al-MCM-41 catalysts

The higher frequency of the IR bands associated to Ni^{2+} in silanols (2197 cm^{-1}) and in small NiO nanoparticles (2185 cm^{-1}) in *x*Ni/Al-M41 with respect to pure silica carriers (2191 cm^{-1} and 2183 cm^{-1}, respectively) point towards some kind of interaction between the Ni^{2+} species and the aluminosilicate matrix promoting the activity of the former. In order to gain some insights into the effect of Al, we performed quantitative ^{27}Al MAS NMR spectroscopy on fully hydrated *x*Ni/Al-M41 samples. The normalized spectra for the bare Al-M41 support and the *x*Ni/Al-M41 samples loaded with different amounts of Ni are given in Fig. 9.

As anticipated, the spectrum of the bare Al-M41 carrier shows a main signal at chemical shift of ~ 52 ppm assigned to framework Al species in a tetrahedral coordination (Al^{IV}) , along with a less intense signal at ~ 0 ppm of six-coordinated Al species (Al^{VI}) in

extraframework positions, representing about 30% of the total Al signal. As observed in Fig. 9, the incorporation of Ni species induced a gradual decrease in the intensity of the two Al signals up to a Ni concentration of 2.8 wt%. At this nickel content, the integrated intensity of the framework Al^{IV} signal was reduced by about 45% with respect to the pristine Al-M41 support, while that of the extraframework Al^{VI} species practically vanished. Increasing further the nickel content in the *x*Ni/Al-M41 samples up to 9.8 wt% did not produce additional changes in the Al signals.

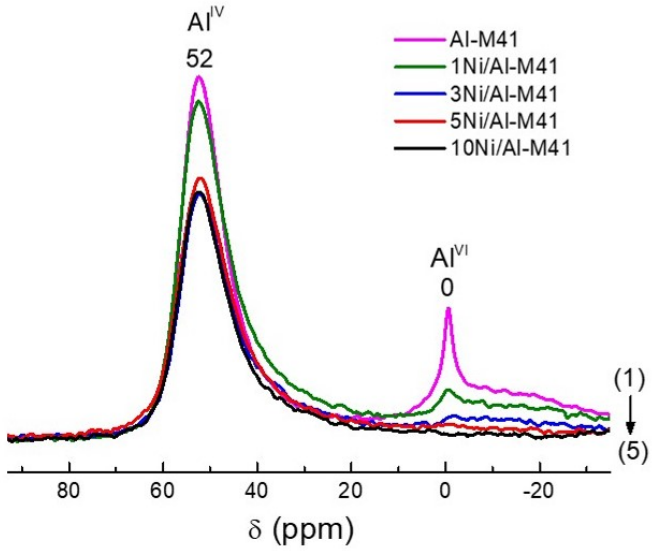

Fig. 9. ^{27}Al MAS NMR spectra of the bare Al-M41 matrix (spectrum 1) and the xNi/Al-M41 catalysts (spectra 2 to 5 in increasing order of Ni loading from 1.3 to 9.8 wt%). The spectra are normalized to sample weight.

The observed reduction of the two Al signals in the presence of nickel could be explained by the close interaction of the Al nuclei with neighboring Ni species with a strong paramagnetic character as a consequence of strong electron-nucleus coupling and short nuclear relaxation times [32,37]. In this regard, small NiO nanoparticles (< 20 nm) are known to exhibit a superparamagnetic behavior, more pronounced at decreasing particle sizes, attributed to the combined effects of lattice distortion and missing bonds affecting their atomic configuration [38,39]. On the other hand, Ni(II) complexes may adopt high-spin (S = 1) or low-spin (S = 0) states depending on the ligand field environment determining their geometrical structure [40] and thus can be paramagnetic or diamagnetic. In Ni-aluminosilicates, isolated Ni^{2+} species were predicted by DFT to be more stable in

the low-spin state, adopting a four-coordinated square planar geometry with two oxide ions of the aluminosilicate framework serving as two of the four ligands [14], and would thus exhibit diamagnetic properties. Considering this, we tentatively attribute the reduction in the intensity of the Al signals observed in the ^{27}Al MAS NMR spectra of *x*Ni/Al-M41 to the interaction of the accessible Al nuclei with nearby paramagnetic small (sub-4 nm) NiO nanoparticles confined within the mesochannels. The fact that a significant fraction of the Al^{IV} species appeared unaffected by the presence of nickel can be attributed to their location at inaccessible positions inside the mesopore walls [41,42]. For instance, in the case of an Al-MCM-41 sample with Si/Al ratio ~ 11, only about 55% of Al atoms were seen to be on the channel surface and thus accessible for catalysis [42].

Further evidence for the interaction between aluminum and nickel species was obtained by FTIR analysis in the OH stretching vibration region after CO adsorption of the activated Al-M41 support and *x*Ni/Al-M41 catalysts. Upon interaction with an OH group, the weak CO base forms an OH···CO adduct that induces a red shift of the O-H stretching vibration (Δν) of silanols, Brønsted acid sites (Si-OH-Al), and extraframework Al-OH species, which extent increases with the acid strength of the concerned OH group. As observed in the difference spectra shown in Fig. 10, the shift decreased in the order: Brønsted acid sites (Δν= 316 cm^{-1}) > Al-OH (Δν= 223-230 cm^{-1}) > silanols (Δν= 98 cm^{-1}), as anticipated from their decreasing acid strength.

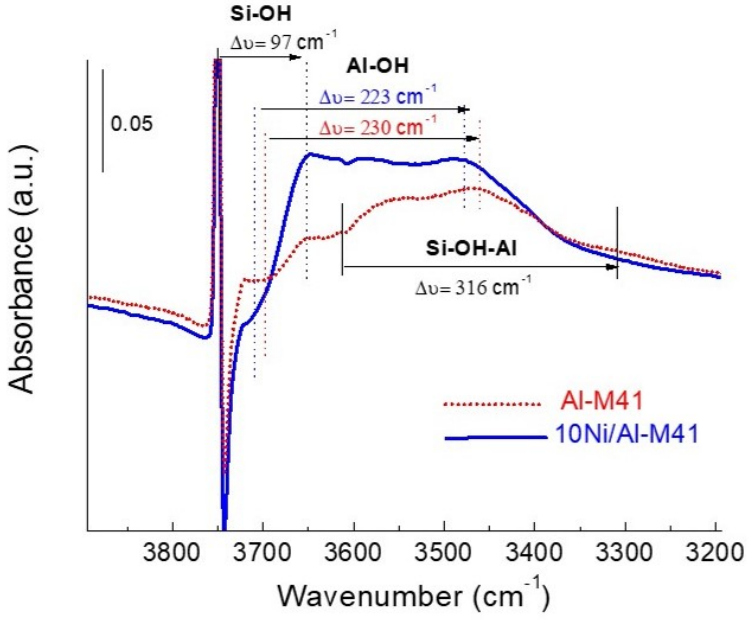

Fig. 10. FTIR difference spectra in the OH stretching region after CO adsorption on activated Al-M41 (solid blue line) and 10Ni/Al-M41 sample (short dotted red line) at low CO coverage. The IR spectra were normalized by sample overtone area.

Interestingly, the Al-OH band in the 10Ni/Al-M41 catalyst experienced a lower shift ($\Delta\nu$= 223 cm^{-1}) than in the Ni-free Al-M41 carrier ($\Delta\nu$=230 cm^{-1}), revealing a lower acidity of the hydroxyl group of Al-OH species (hence, a lower Lewis acid strength of the extraframework Al^{3+} cation) in the Ni-containing sample. This fact might be explained in terms of an electronic charge transfer to the Lewis acid Al^{3+} cations from the Lewis basic oxygen atoms linked to nearby Ni^{2+} species, which could account, at least in part, for the observed red shift of the related Ni^{2+}-carbonyl IR bands in the aluminosilicate Al-M41 with respect to the pure silica samples.

The electronic interaction between the Lewis acid Al^{3+} and Ni^{2+} cations through the basic oxygen nickel ligands is schematically exemplified in Fig. 11 for the Ni^{2+} species grafted on silanols as one of the possible mechanisms for the promoting effect of Al species.

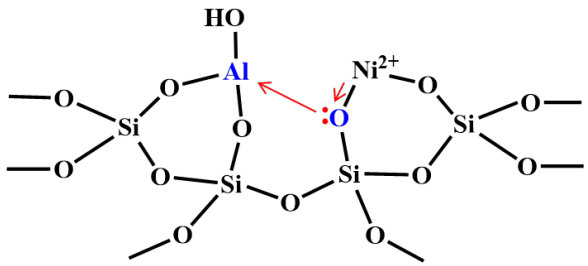

Fig. 11. Schematic illustration of the electronic interaction between electron-withdrawing Al^{3+} species and vicinal oxygen atoms of silanol groups enhancing the Lewis acidity of grafted Ni^{2+} sites.

Overall, the ^{27}Al MAS NMR and FTIR results discussed before sign for a close interaction between the Al species in the aluminosilicate matrix and the Ni^{2+} species in the *x*Ni/Al-M41 catalysts enhancing the Lewis acid strength of the later. This interaction might explain, at least in part, the higher reactivity of the unsaturated Ni^{2+} species grafted in silanols and on the surface of small confined NiO nanoparticles, suggested here as the

active nickel species in *working* Ni-Al-MCM-41 catalysts, in comparison with Ni on silica carriers.

4. CONCLUSIONS

In this work, we applied in situ time-resolved FTIR spectroscopy of adsorbed CO in combination with reaction kinetics (both at 120 °C and 1 bar) to elucidate the nature of active nickel sites in Ni/Al-MCM-41 catalysts (1.3 – 9.8 wt% Ni) during the oligomerization of ethylene. These experiments revealed a fast initial decline in activity due to the rapid blockage of ion-exchanged Ni^{2+} species (IR band at 2207 cm^{-1}), the previously assumed active sites, by irreversibly adsorbed hydrocarbon species. Consequently, only Ni^{2+} ions grafted on silanols and at the surface of small in-pore NiO nanoparticles characterized by, respectively, IR bands at 2197 and 2185 cm^{-1} remain available for reaction and are thus proposed here as the active nickel species operating in the *pseudo*-steady state. At identical reaction conditions, however, these nickel species exhibited a remarkably lower steady state activity when present in pure silica materials in comparison with Ni/Al-MCM-41 catalysts with equivalent Ni loading. Moreover, FTIR-CO spectroscopy showed a shift towards lower frequencies of the nickel carbonyl IR bands associated to grafted Ni^{2+} ions and in-pore NiO nanoparticles in the pure silica materials with respect to the aluminosilicate counterparts. This result indicated a lower Lewis acid strength of the nickel species in all-silica catalysts and evidenced a crucial role of Al species in the aluminosilicate matrix in promoting the Lewis acidity and, consequently, the catalytic activity of the proposed active nickel sites. In this regard, both quantitative ^{27}Al MAS NMR and FTIR in the OH region after CO adsorption evidenced a close interaction between Al and Ni species in Ni/Al-M41. As one of the possible promotion mechanisms, FTIR revealed a synergic electronic effect of Lewis acid extraframework Al^{3+} species by which the electron density of nearby Ni^{2+} ions is reduced enhancing their electrophilic character (i.e., Lewis acid strength) and, as a result, their ability to coordinate and activate ethylene at mild conditions.

Acknowledgments

This work has been financially supported by the Spanish government through the Severo Ochoa Program (SEV2016-0683) and RTI2018-102161 projects. The authors

acknowledge the Microscopy Service of the Universitat Politècnica de València for its assistance in the characterization of materials by electron microscopy.

References

[1] W. Keim, Oligomerization of ethylene to α-olefins: Discovery and development of the shell higher olefin process (SHOP), Angew. Chemie - Int. Ed. (2013) 12492–12496. https://doi.org/10.1002/anie.201305308.

[2] J. Skupinska, Oligomerization of a-Olefins to Higher Oligomers, 1991. https://pubs.acs.org/sharingguidelines.

[3] A. Finiels, F. Fajula, V. Hulea, Nickel-based solid catalysts for ethylene oligomerization-a review, Catal. Sci. Technol. (2014). https://doi.org/10.1039/c4cy00305e.

[4] S. Moussa, M.A. Arribas, P. Concepción, A. Martínez, Heterogeneous oligomerization of ethylene to liquids on bifunctional Ni-based catalysts: The influence of support properties on nickel speciation and catalytic performance, Catal. Today. 277 (2016) 78–88. https://doi.org/10.1016/j.cattod.2015.11.032.

[5] F. Jin, Y. Yan, G. Wu, Ethylene oligomerization over H- and Ni-form aluminosilicate composite with ZSM-5 and MCM-41 structure: Effect of acidity strength, nickel site and porosity, Catal. Today. (2019). https://doi.org/10.1016/j.cattod.2019.06.050.

[6] A. Martínez, M.A. Arribas, P. Concepción, S. Moussa, New bifunctional Ni-H-Beta catalysts for the heterogeneous oligomerization of ethylene, Appl. Catal. A Gen. (2013). https://doi.org/10.1016/j.apcata.2013.08.021.

[7] T. Yashima, Y. Ushida, M. Ebisawa, N. Hara, Polymerization of ethylene over transition-metal exchanged Y zeolites, J. Catal. 36 (1975) 320–326. https://doi.org/https://doi.org/10.1016/0021-9517(75)90042-1.

[8] M. Hartmann, A. Pöppl, L. Kevan, Ethylene dimerization and butene isomerization in nickel-containing MCM-41 and AlMCM-41 mesoporous molecular sieves: An electron spin resonance and gas chromatography study, J. Phys. Chem. (1996). https://doi.org/10.1021/jp9602181.

[9] I. V. Elev, B.N. Shelimov, V.B. Kazansky, The Role of Ni+ Ions in the activity of

NiCaY Zeolite catalysts for Ethylene Dimerization, J. Catal. (1984). https://doi.org/10.1016/0021-9517(84)90323-3.

[10] M. Hartmann, A. Poeppl, L. Kevan, Formation and stability of Ni(I) ions in MCM-41 mesoporous molecular sieves, J. Phys. Chem. (1995). https://doi.org/10.1021/j100049a004.

[11] F.T.T. Ng, D.C. Creaser, Ethylene dimerization over modified nickel exchanged Y-zeolite, Appl. Catal. A, Gen. (1994). https://doi.org/10.1016/0926-860X(94)85200-6.

[12] M. Tanaka, A. Itadani, Y. Kuroda, M. Iwamoto, Effect of pore size and nickel content of Ni-MCM-41 on catalytic activity for ethene dimerization and local structures of nickel ions, J. Phys. Chem. C. (2012). https://doi.org/10.1021/jp2103066.

[13] S. Moussa, P. Concepción, M.A. Arribas, A. Martínez, Nature of Active Nickel Sites and Initiation Mechanism for Ethylene Oligomerization on Heterogeneous Ni-beta Catalysts, ACS Catal. (2018). https://doi.org/10.1021/acscatal.7b03970.

[14] R.Y. Brogaard, U. Olsbye, Ethene Oligomerization in Ni-Containing Zeolites: Theoretical Discrimination of Reaction Mechanisms, ACS Catal. 6 (2016) 1205–1214. https://doi.org/10.1021/acscatal.5b01957.

[15] K. Toch, J.W. Thybaut, G.B. Marin, Ethene oligomerization on Ni-SiO2-Al2O3: Experimental investigation and Single-Event MicroKinetic modeling, Appl. Catal. A Gen. 489 (2015) 292–304. https://doi.org/10.1016/j.apcata.2014.10.036.

[16] R.D. Andrei, M.I. Popa, F. Fajula, V. Hulea, Heterogeneous oligomerization of ethylene over highly active and stable Ni-AlSBA-15 mesoporous catalysts, J. Catal. (2015). https://doi.org/10.1016/j.jcat.2014.12.027.

[17] R.Y. Brogaard, M. Kømurcu, M.M. Dyballa, A. Botan, V. Van Speybroeck, U. Olsbye, K. De Wispelaere, Ethene Dimerization on Zeolite-Hosted Ni Ions: Reversible Mobilization of the Active Site, ACS Catal. 9 (2019) 5645–5650. https://doi.org/10.1021/acscatal.9b00721.

[18] A. Corma, V. Fornes, M.T. Navarro, J. Perezpariente, Acidity and Stability of MCM-41 Crystalline Aluminosilicates, J. Catal. 148 (1994) 569–574. https://doi.org/https://doi.org/10.1006/jcat.1994.1243.

[19] K. Hadjiivanov, M. Mihaylov, D. Klissurski, P. Stefanov, N. Abadjieva, E. Vassileva, L. Mintchev, Characterization of Ni/SiO2 Catalysts Prepared by Successive Deposition and Reduction of Ni2+ Ions, J. Catal. 185 (1999) 314–323. https://doi.org/https://doi.org/10.1006/jcat.1999.2521.

[20] M. Kruk, M. Jaroniec, A. Sayari, Application of large pore MCM-41 molecular sieves to improve pore size analysis using nitrogen adsorption measurements, Langmuir. (1997). https://doi.org/10.1021/la970776m.

[21] V. Zholobenko, C. Freitas, M. Jendrlin, P. Bazin, A. Travert, F. Thibault-Starzyk, Probing the acid sites of zeolites with pyridine: Quantitative AGIR measurements of the molar absorption coefficients, J. Catal. 385 (2020) 52–60. https://doi.org/https://doi.org/10.1016/j.jcat.2020.03.003.

[22] V. Hulea, F. Fajula, Ni-exchanged AlMCM-41 - An efficient bifunctional catalyst for ethylene oligomerization, J. Catal. 225 (2004) 213–222. https://doi.org/10.1016/j.jcat.2004.04.018.

[23] A. Lewandowska, S. Monteverdi, M. Bettahar, M. Ziolek, MCM-41 mesoporous molecular sieves supported nickel—physico-chemical properties and catalytic activity in hydrogenation of benzene, J. Mol. Catal. A Chem. 188 (2002) 85–95. https://doi.org/https://doi.org/10.1016/S1381-1169(02)00339-4.

[24] R. Wojcieszak, S. Monteverdi, M. Mercy, I. Nowak, M. Ziolek, M.M. Bettahar, Nickel containing MCM-41 and AlMCM-41 mesoporous molecular sieves: Characteristics and activity in the hydrogenation of benzene, Appl. Catal. A Gen. 268 (2004) 241–253. https://doi.org/https://doi.org/10.1016/j.apcata.2004.03.047.

[25] X.-Y. Quek, D. Liu, W.N.E. Cheo, H. Wang, Y. Chen, Y. Yang, Nickel-grafted TUD-1 mesoporous catalysts for carbon dioxide reforming of methane, Appl. Catal. B Environ. 95 (2010) 374–382. https://doi.org/https://doi.org/10.1016/j.apcatb.2010.01.016.

[26] E. Lovell, Y. Jiang, J. Scott, F. Wang, Y. Suhardja, M. Chen, J. Huang, R. Amal, CO2 reforming of methane over MCM-41-supported nickel catalysts: altering support acidity by one-pot synthesis at room temperature, Appl. Catal. A Gen. 473 (2014) 51–58. https://doi.org/https://doi.org/10.1016/j.apcata.2013.12.020.

[27] D.J. Lensveld, J. Gerbrand Mesu, A. Jos van Dillen, K.P. de Jong, Synthesis and

characterisation of MCM-41 supported nickel oxide catalysts, Microporous Mesoporous Mater. 44–45 (2001) 401–407. https://doi.org/https://doi.org/10.1016/S1387-1811(01)00214-1.

[28] K. Góra-Marek, J. Datka, IR studies of OH groups in mesoporous aluminosilicates, Appl. Catal. A Gen. 302 (2006) 104–109. https://doi.org/https://doi.org/10.1016/j.apcata.2005.12.027.

[29] E. J.M. Hensen, D. G. Poduval, V. Degirmenci, D.. J. Michel Ligthart, W. Chen, F. Maugé, M. S. Rigutto, J.A. Rob van Veen, Acidity Characterization of Amorphous Silica–Alumina, J. Phys. Chem. C. 116 (2012) 21416–21429. https://doi.org/10.1021/jp309182f.

[30] R. Henry, M. Komurcu, Y. Ganjkhanlou, R.Y. Brogaard, L. Lu, K.-J. Jens, G. Berlier, U. Olsbye, Ethene oligomerization on nickel microporous and mesoporous-supported catalysts: Investigation of the active sites, Catal. Today. 299 (2018) 154–163. https://doi.org/10.1016/j.cattod.2017.04.029.

[31] K. Góra-Marek, A. Glanowska, J. Datka, Quantitative IR studies of the concentration of different nickel sites in NiZSM-5 zeolites, Microporous Mesoporous Mater. 158 (2012) 162–169. https://doi.org/https://doi.org/10.1016/j.micromeso.2012.03.027.

[32] M. Mihaylov, K. Hadjiivanov, FTIR Study of CO and NO Adsorption and Coadsorption on Ni-ZSM-5 and Ni/SiO2, Langmuir. 18 (2002) 4376–4383. https://doi.org/10.1021/la015739g.

[33] M. Lallemand, O.A. Rusu, E. Dumitriu, A. Finiels, F. Fajula, V. Hulea, NiMCM-36 and NiMCM-22 catalysts for the ethylene oligomerization: Effect of zeolite texture and nickel cations/acid sites ratio, Appl. Catal. A Gen. 338 (2008) 37–43. https://doi.org/10.1016/j.apcata.2007.12.024.

[34] M. Lallemand, A. Finiels, F. Fajula, V. Hulea, Catalytic oligomerization of ethylene over Ni-containing dealuminated Y zeolites, Appl. Catal. A Gen. 301 (2006) 196–201. https://doi.org/10.1016/j.apcata.2005.12.019.

[35] J. Heveling, C.P. Nicolaides, M.S. Scurrell, Catalysts and conditions for the highly efficient, selective and stable heterogeneous oligomerisation of ethylene, Appl. Catal. A Gen. 173 (1998) 1–9. https://doi.org/https://doi.org/10.1016/S0926-

860X(98)00147-1.

[36] A. Penkova, S. Dzwigaj, R. Kefirov, K. Hadjiivanov, M. Che, Effect of the Preparation Method on the State of Nickel Ions in BEA Zeolites. A Study by Fourier Transform Infrared Spectroscopy of Adsorbed CO and NO, Temperature-Programmed Reduction, and X-Ray Diffraction, J. Phys. Chem. C. 111 (2007) 8623–8631. https://doi.org/10.1021/jp071927p.

[37] V.I. Bakhmutov, B.G. Shpeizer, A. V Prosvirin, K.R. Dunbar, A. Clearfield, Supermicroporous silica-based SiO2–Al2O3–NiO materials: Solid-state NMR, NMR relaxation and magnetic susceptibility, Microporous Mesoporous Mater. 118 (2009) 78–86. https://doi.org/https://doi.org/10.1016/j.micromeso.2008.08.023.

[38] H. Bi, S. Li, Y. Zhang, Y. Du, Ferromagnetic-like behavior of ultrafine NiO nanocrystallites, J. Magn. Magn. Mater. 277 (2004) 363–367. https://doi.org/https://doi.org/10.1016/j.jmmm.2003.11.017.

[39] S.S. Nkosi, B. Yalisi, D.E. Motaung, J. Keartland, E. Sideras-Haddad, A. Forbes, B.W. Mwakikunga, Antiferromagnetic–paramagnetic state transition of NiO synthesized by pulsed laser deposition, Appl. Surf. Sci. 265 (2013) 860–864. https://doi.org/https://doi.org/10.1016/j.apsusc.2012.11.134.

[40] G. Piao, K. Akagi, H. Shirakawa, Spin structures and properties of paramagnetic nickel(II) complexes with liquid crystalline β-diketone ligands, Synth. Met. 85 (1997) 1669–1670. https://doi.org/https://doi.org/10.1016/S0379-6779(97)80390-6.

[41] C. Perego, R. Millini, Porous materials in catalysis: challenges for mesoporous materials, Chem. Soc. Rev. 42 (2013) 3956–3976. https://doi.org/10.1039/C2CS35244C.

[42] J. Dědeček, N. Žilková, J. Čejka, Experimental study of the effect of Si/Al composition on the aluminum distribution in (Al)MCM-41, Microporous Mesoporous Mater. 44–45 (2001) 259–266. https://doi.org/https://doi.org/10.1016/S1387-1811(01)00191-3.

Supplementary Material

The nature of active Ni sites and the role of Al species in the oligomerization of ethylene on mesoporous Ni-Al-MCM-41 catalysts

Sara Moussa, Patricia Concepción, Maria A. Arribas, and Agustín Martínez*

Instituto de Tecnología Química, Universitat Politècnica de València - Consejo Superior de Investigaciones Científicas (UPV-CSIC), Avda. de los Naranjos s/n, 46022 Valencia, Spain.

*Corresponding author: amart@itq.upv.es (A. Martínez)

Table S1. Initial (TOS = 1 min) and *pseudo*-steady state (TOS = 60 min) carbon number distribution of oligomers (in wt%) for *x*Ni/Al-M41 catalysts with different Ni content in the ethylene oligomerization experiments performed at 120 °C, 1 bar total presure (0.95 bar ethylene, balanced by Ar), and WHSV of 33 h^{-1}. No products higher than C_8 were found at these reaction conditions.

	1Ni/Al-M41		3Ni/Al-M41		5Ni/Al-M41		10Ni/Al-M41	
	Initial	SS[a]	Initial	SS[a]	Initial	SS[a]	Initial	SS[a]
X_{ethyl}[b] (%)	7.1	2.1	9.0	2.8	10.3	3.1	10.8	3.2
Oligomer distribution (wt%)								
$C_4^=$	88.4	92.0	87.5	91.8	87.8	91.7	87.7	91.4
$C_5^=$	1.5	0.3	1.3	0.2	1.1	0.2	1.1	0.2
$C_6^=$	7.1	6.7	8.1	7.0	8.3	6.8	8.3	7.2
$C_7^=$	0.6	0.0	0.6	0.0	0.5	0.0	0.5	0.0
$C_8^=$	2.4	1.0	2.5	1.0	2.3	1.3	2.4	1.2

[a] SS: *pseudo*-steady state. [b] Conversion of ethylene.

Table S2. Carbon number distribution of oligomers (in wt%) in the *pseudo*-steady state for *x*Ni/Al-M41 catalysts obtained in the high-pressure ethylene oligomerization experiments. Reaction conditions: 120 °C, 35 bar total presure (26 bar ethylene, balanced by Ar), and WHSV of 10 h^{-1}.

Catalyst	1Ni/Al-M41	3Ni/Al-M41	5Ni/Al-M41	10Ni/Al-M41
X_{ethyl} (%)	41.6	77.8	91.2	92.7
Oligomer distribution (wt%)				
$C_4^=$	60.7	56.8	49.8	41.6
$C_5^=$	0.4	0.4	0.5	0.4
$C_6^=$	9.9	13.3	15.5	16.0
$C_7^=$	0.2	0.2	0.2	0.2
$C_8^=$	8.4	11.8	13.7	13.3
$C_9^=$	0.5	0.4	0.4	0.3
$C_{10}^=$	7.3	8.8	10.3	11.8
$C_{11}^=$	0.5	0.2	0.2	0.3
$C_{12}^=$	7.2	4.6	5.1	9.5
$C_{13+}^=$	4.9	3.5	4.3	6.6

Fig. S1. Reproducibility of catalytic experiments at high and ambient pressure conditions over selected *x*Ni/Al-M41 catalysts.

A) Ethylene conversion-TOS curves (a) and product distribution in the steady state (b) at 120 °C, 35 bar, and WHSV of 10 h^{-1} for catalyst 5Ni/Al-M41.

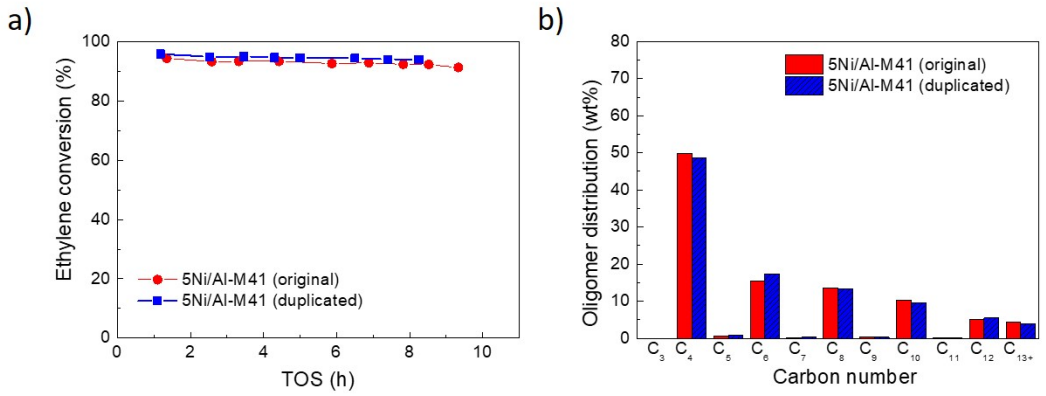

B) Ethylene conversion-TOS curves (a) and product distribution in the steady state (b) at 120 °C, 1 bar, and WHSV of 33 h^{-1} for catalyst 10Ni/Al-M41.

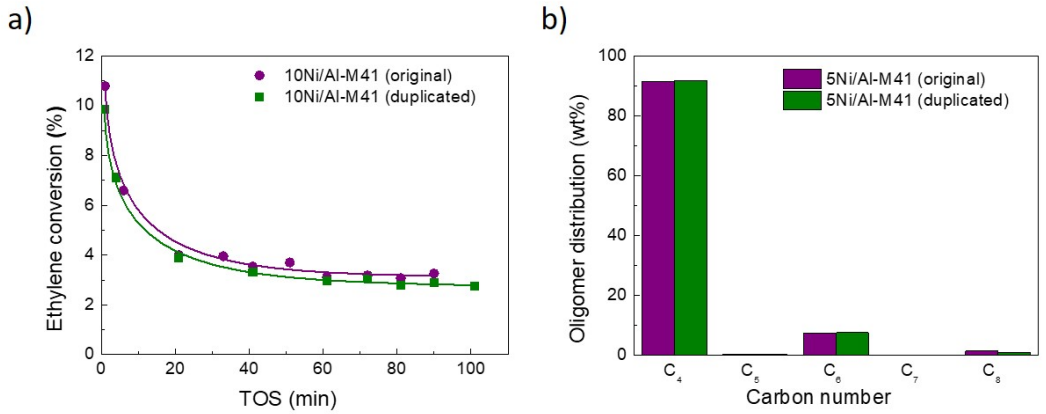

Fig. S2. Low-angle XRD patterns of Al-M41 support and impregnated xNi/Al-M41 catalysts with different Ni loading.

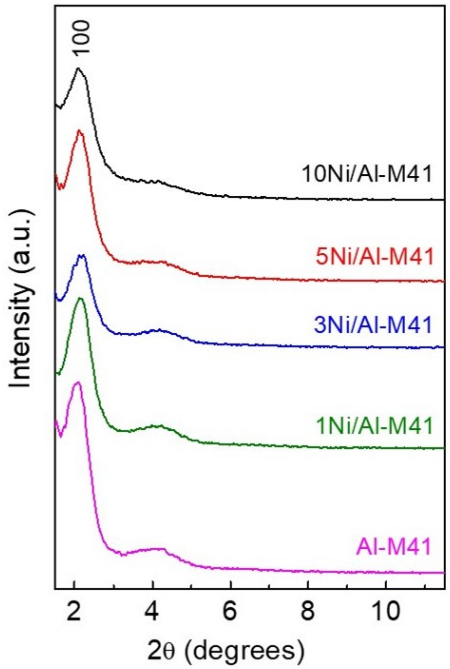

Fig. S3. Nitrogen adsorption isotherms (a) and BJH-KJS pore size distributions (b) for the Al-M41 carrier and *x*Ni/Al-M41 catalysts. For the sake of clarity, the isotherms for samples 1Ni/Al-M41, 3Ni/Al-M41, 5Ni/Al-M41, and 10Ni/Al-M41 have been up-shifted by, respectively, 110, 194, 320, and 451 cm^3/g.

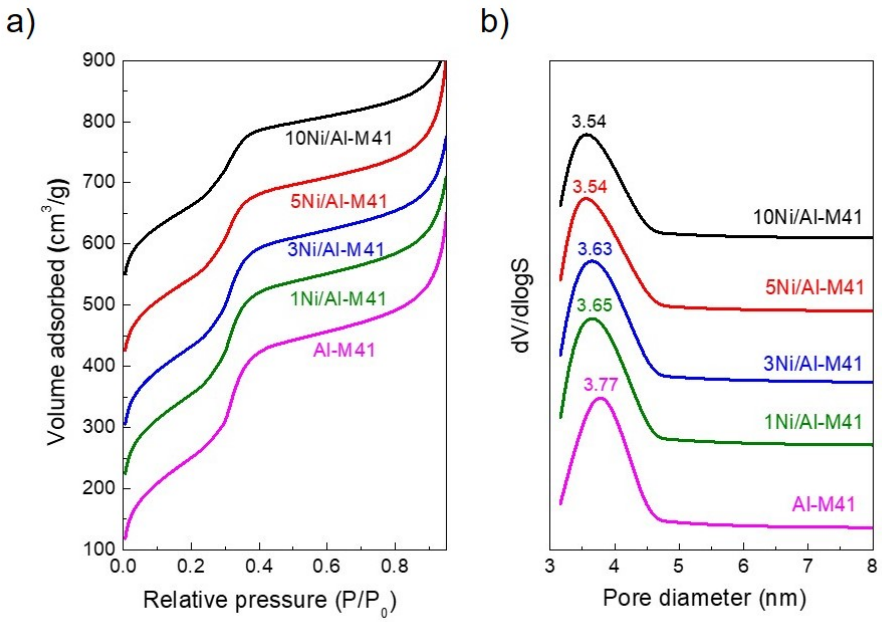

Fig. S4. High-angle XRD patterns of impregnated *x*Ni/Al-41 catalysts with different Ni loadings.

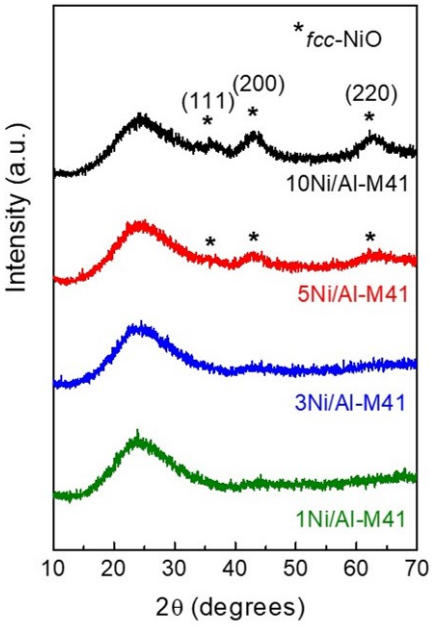

Fig. S5. H_2-TPR profile of NiO crystallites with average particle size of 30 nm physically mixed with the Al-MCM-41 support to obtain a Ni content of 5 wt%.

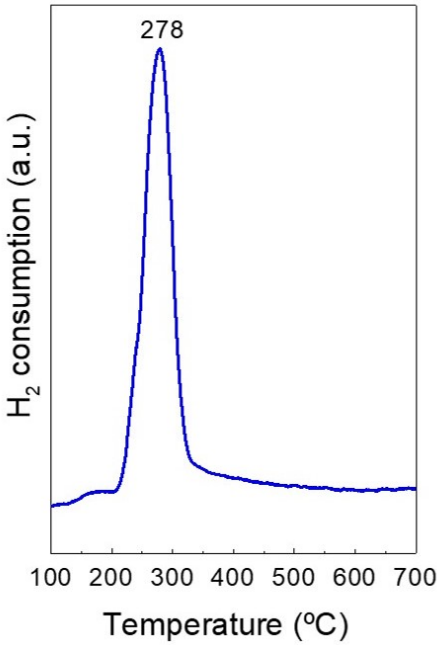

Fig. S6. Deconvoluted H_2-TPR profiles for catalysts 1Ni/Al-M41 (1.3 wt% Ni), 3Ni/Al-M41 (2.8 wt% Ni), and 5Ni/Al-M41 (5.7 wt% Ni).

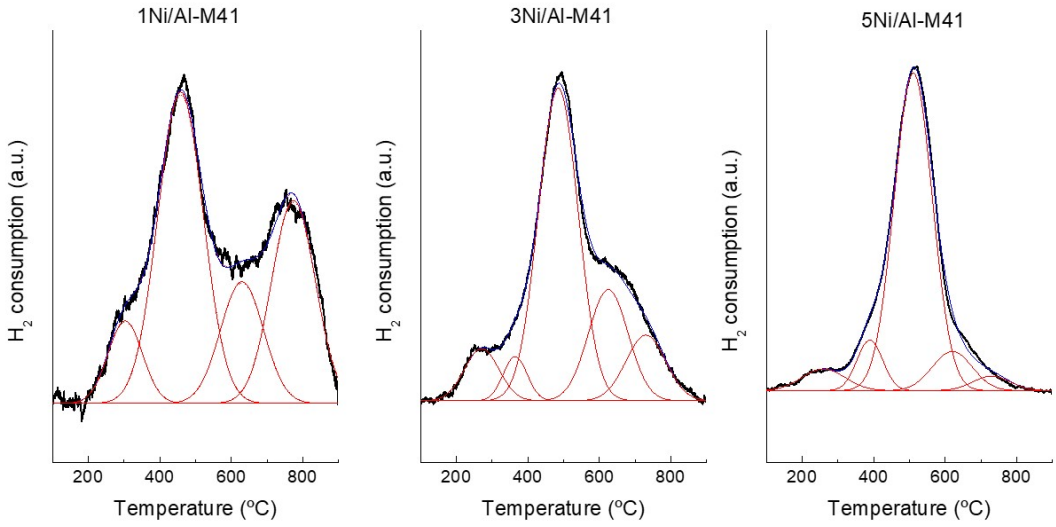

Fig. S7. TEM image of NiO nanoparticles in the impregnated 1Ni/Al-M41 catalyst with Fast Fourier Transform (FFT) analysis of a selected nanoparticle.

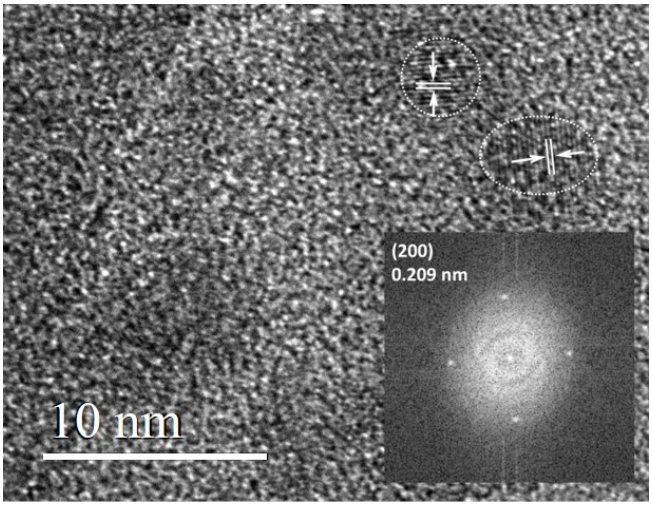

A lattice spacing of 0.209 nm was determined by FFT, in line with the theoretical value (0.2084 nm) of the (200) plane of *fcc*-NiO nanoparticles.

Fig. S8. a) FTIR spectra of adsorbed CO at increasing CO dosing (0.14 – 2.0 mbar) for the impregnated 5Ni/Al-M41 sample; b) second derivative curves for selected spectra.

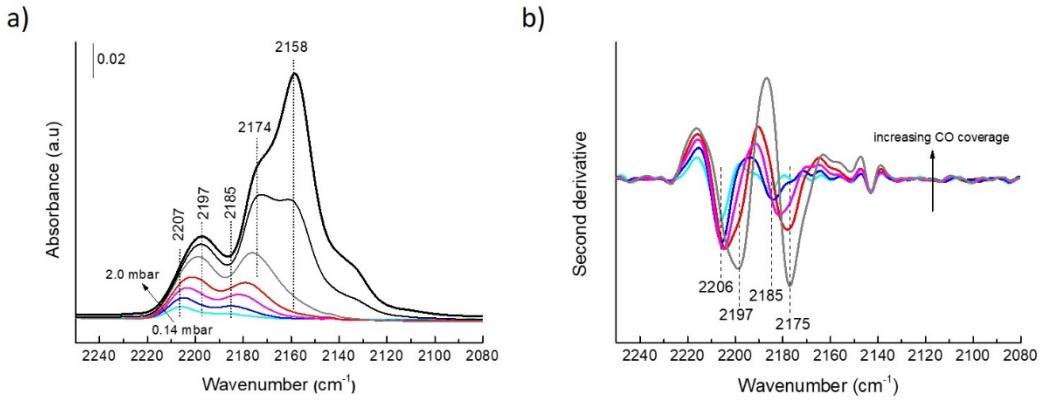

Fig. S9. Deconvoluted FTIR-CO spectrum at CO saturation of Ni-carbonyls of an Al-free Ni-Si-M41 sample (1.7 wt% Ni) prepared by grafting (see main text) after thermal treatment in flowing N_2 at 300 ºC. Only the region of Ni-carbonyls is shown for the sake of clarity.

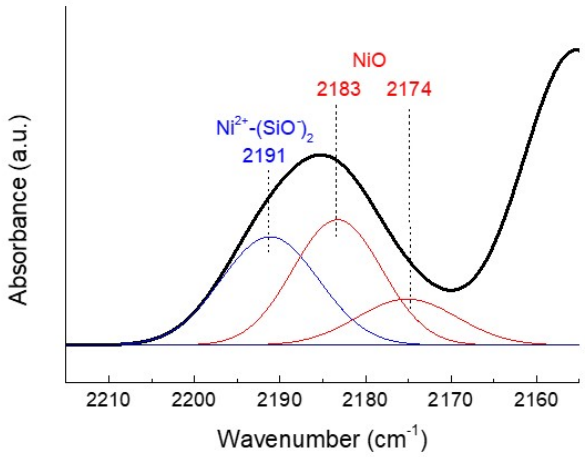

Fig. S10. Evolution with Ni loading of the integrated area of the different Ni^{2+}-CO IR bands (ion-exchanged: 2207 cm^{-1}, grafted on silanols: 2197 cm^{-1}, NiO: 2185 cm^{-1}) for thermally treated (N_2, 300 °C) *x*Ni/Al-M41 catalysts assessed from the deconvoluted IR spectra at CO saturation of Ni-carbonyl bands.

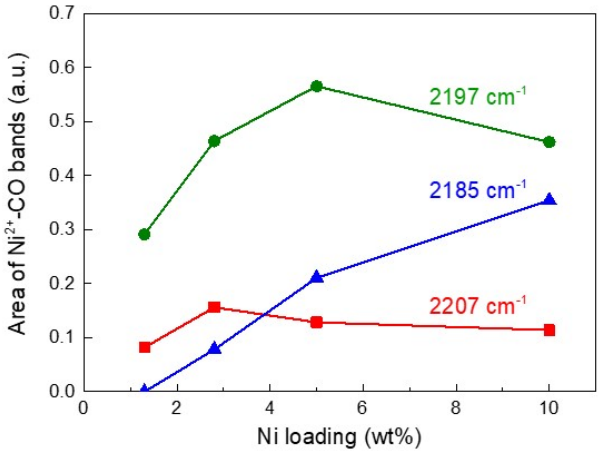

Fig. S11. Ethylene conversion rate as a function of TOS (a) and of Ni loading at TOS of 1 min and > 60 min (b) for *x*Ni/Al-M41 catalysts. Reaction conditions: 120 °C, 1 bar total pressure (0.95 bar ethylene + 0.05 bar Ar), and WHSV of 33 h^{-1}.

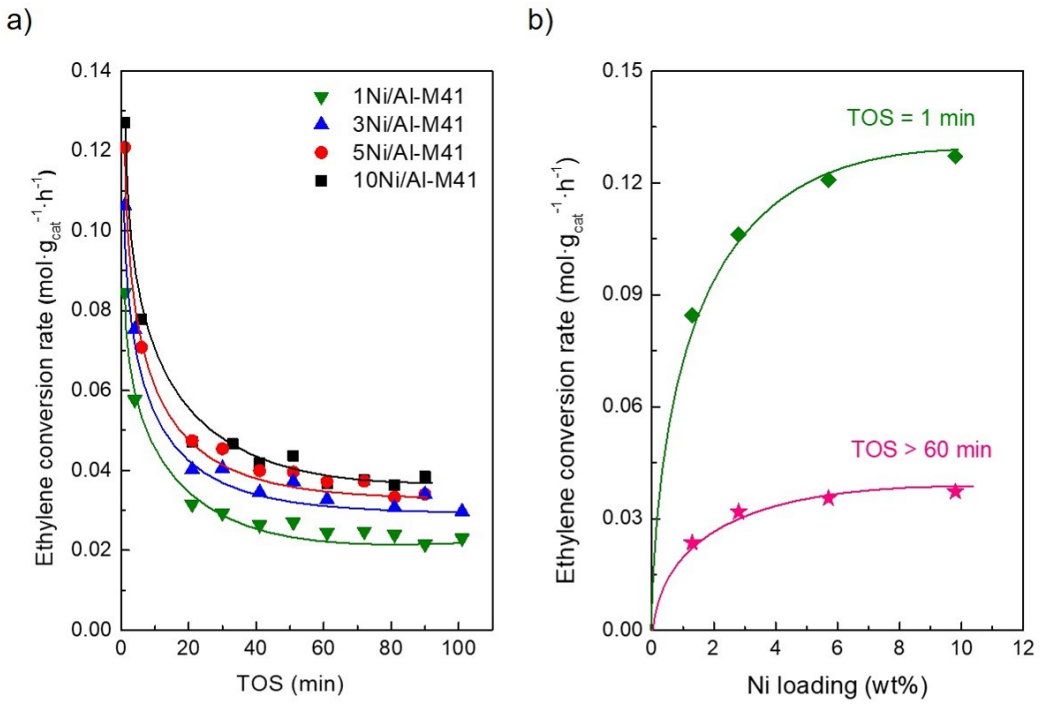

Fig. S12. Evolution of ethylene conversion with TOS for *x*Ni/Al-M41 catalysts at 120 °C, 35 bat total pressure (26 bar ethylene), and WHSV of 10 h^{-1}.

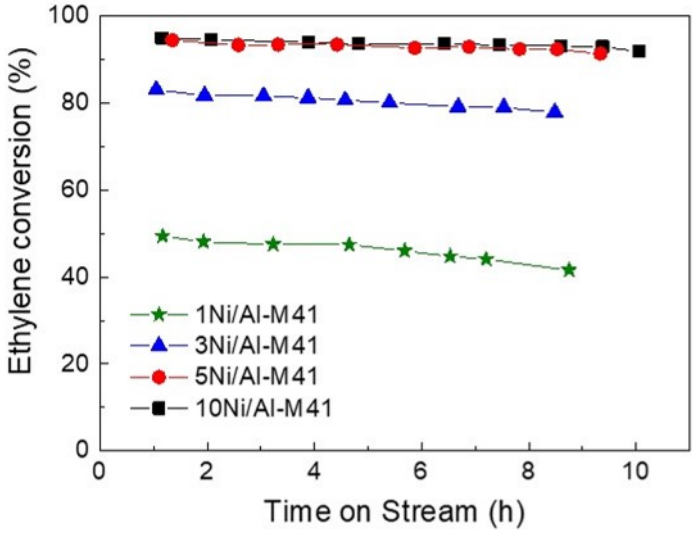

Fig. S13. (a) FTIR spectrum at CO saturation of Ni-carbonyl bands for 5Ni/Al-M41 catalyst after 70 min of in situ reaction with ethylene at 120 °C and 1 bar, and (b) second derivative curve.

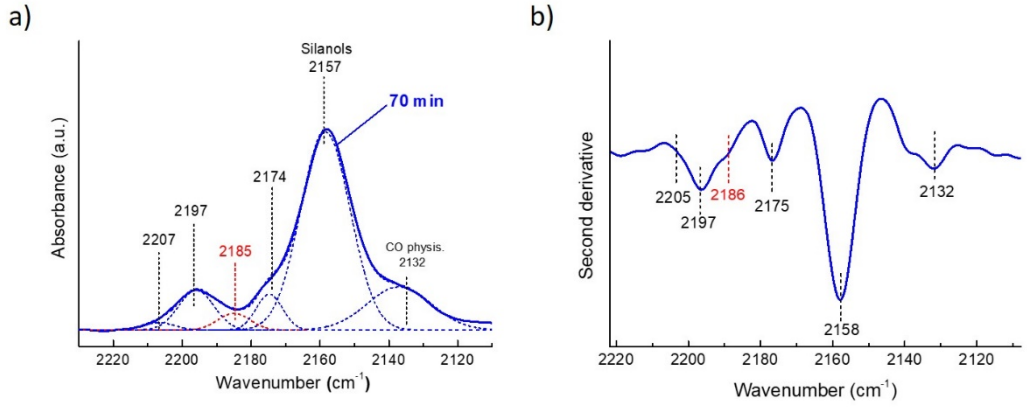

Fig. S14. FTIR spectra at CO saturation of Ni-carbonyl bands for 3Ni/Al-M41 catalyst after the pretreatment in N_2 at 300 °C (0 min) and after 70 min of in situ reaction with ethylene at 120 ºC and 1 bar.

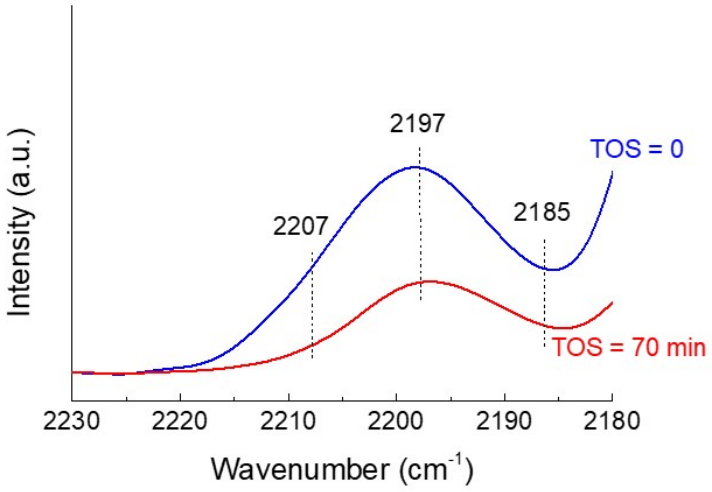

Fig. S15. FTIR spectra in the C-H stretching (a) and bending (b) vibration regions for the 5Ni/Al-M41 catalyst after the thermal treatment at 300 °C (0 min) and after reaction with ethylene at 120 ºC and 1 bar for 1 and 70 min and subsequent evacuation of the cell at 120 ºC for 1 h under dynamic vacuum of 10^{-5} mbar. The IR spectra were normalized by sample overtone area.

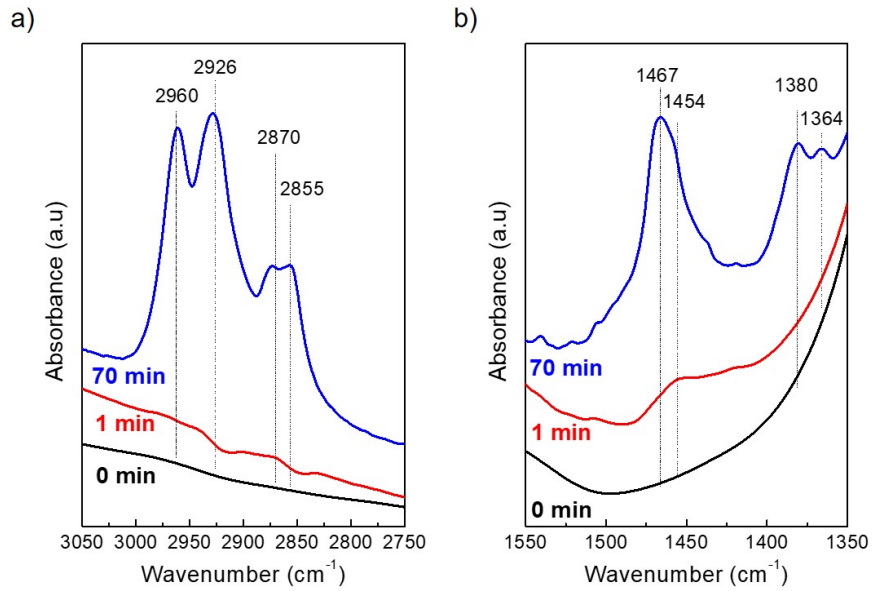

As shown in the figures, characteristic C-H stretching and bending IR bands of CH_3 (ν_{as}= 2960 cm^{-1}, ν_s= 2870 cm^{-1}, δ_s= 1364 – 1380 cm^{-1}, δ_{as}= 1440 – 1470 cm^{-1}) and CH_2 (ν_{as}= 2926 cm^{-1}, ν_s= 2855 cm^{-1}, δ= 1440 – 1470 cm^{-1}) groups are observed.

Fig. S16. Low- (a) and high-angle (b) XRD patterns of Ni catalysts grafted on silica materials: Ni-Si-M41 (1.7 wt% Ni) and NiO-SiO_2 (2.7 wt% Ni).

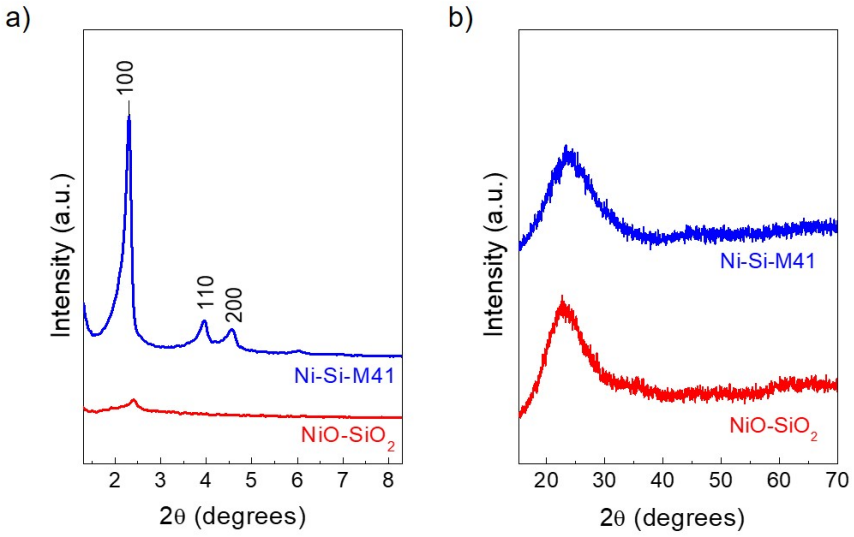

Fig. S17. Representative STEM image showing the presence of small (2 – 5 nm) NiO nanoparticles in the Al-free NiO-SiO_2 sample.